Search for dark matter with a 231-day exposure of liquid argon using DEAP-3600 at SNOLAB

Article (Published Version)

Search for dark matter with a 231-day exposure of liquid argon using DEAP-3600 at SNOLAB

R. Ajaj,[3] P.-A. Amaudruz,[17] G. R. Araujo,[7] M. Baldwin,[14] M. Batygov,[5] B. Beltran,[1] C. E. Bina,[1] J. Bonatt,[12] M. G. Boulay,[3,12] B. Broerman,[12] J. F. Bueno,[1] P. M. Burghardt,[7] A. Butcher,[13] B. Cai,[12] S. Cavuoti,[9,8] M. Chen,[12] Y. Chen,[1] B. T. Cleveland,[15,5] D. Cranshaw,[12] K. Dering,[12] J. DiGioseffo,[3] L. Doria,[11] F. A. Duncan,[15,*] M. Dunford,[3] A. Erlandson,[3,2] N. Fatemighomi,[15,13] G. Fiorillo,[9,8] S. Florian,[12] A. Flower,[3,12] R. J. Ford,[15,5] R. Gagnon,[12] D. Gallacher,[3] E. A. Garcés,[6] S. Garg,[3] P. Giampa,[17,12] D. Goeldi,[3] V. V. Golovko,[2] P. Gorel,[15,5,1] K. Graham,[3] D. R. Grant,[1] A. L. Hallin,[1] M. Hamstra,[3,12] P. J. Harvey,[12] C. Hearns,[12] A. Joy,[1] C. J. Jillings,[15,5] O. Kamaev,[2] G. Kaur,[3] A. Kemp,[13] I. Kochanek,[4] M. Kuźniak,[3,12] S. Langrock,[5] F. La Zia,[13] B. Lehnert,[3] X. Li,[10] J. Lidgard,[12] T. Lindner,[17] O. Litvinov,[17] J. Lock,[3] G. Longo,[9,8] P. Majewski,[14] A. B. McDonald,[12] T. McElroy,[1] T. McGinn,[3,12,*] J. B. McLaughlin,[13,12] R. Mehdiyev,[3] C. Mielnichuk,[1] J. Monroe,[13] P. Nadeau,[3] C. Nantais,[12] C. Ng,[1] A. J. Noble,[12] E. O'Dwyer,[12] C. Ouellet,[3] P. Pasuthip,[12] S. J. M. Peeters,[16] M.-C. Piro,[1] T. R. Pollmann,[7] E. T. Rand,[2] C. Rethmeier,[3] F. Retière,[17] N. Seeburn,[13] K. Singhrao,[1] P. Skensved,[12] B. Smith,[17] N. J. T. Smith,[15,5] T. Sonley,[3,15] J. Soukup,[1] R. Stainforth,[3] C. Stone,[12] V. Strickland,[17,3] B. Sur,[2] J. Tang,[1] E. Vázquez-Jáuregui,[6] L. Veloce,[12] S. Viel,[3] J. Walding,[13] M. Waqar,[3] M. Ward,[12] S. Westerdale,[3] J. Willis,[1] and A. Zuñiga-Reyes[6]

(DEAP Collaboration)[†]

[1]*Department of Physics, University of Alberta, Edmonton, Alberta, T6G 2R3, Canada*
[2]*Canadian Nuclear Laboratories Limited, Chalk River, Ontario, K0J 1J0, Canada*
[3]*Department of Physics, Carleton University, Ottawa, Ontario, K1S 5B6, Canada*
[4]*INFN Laboratori Nazionali del Gran Sasso, Assergi (AQ) 67100, Italy*
[5]*Department of Physics and Astronomy, Laurentian University, Sudbury, Ontario, P3E 2C6, Canada*
[6]*Instituto de Física, Universidad Nacional Autónoma de México, A. P. 20-364, México D. F. 01000, Mexico*
[7]*Department of Physics, Technische Universität München, 80333 Munich, Germany*
[8]*INFN Napoli, Napoli 80126, Italy*
[9]*Physics Department, Università degli Studi "Federico II" di Napoli, Napoli 80126, Italy*
[10]*Physics Department, Princeton University, Princeton, New Jersey 08544, USA*
[11]*PRISMA Cluster of Excellence and Institut für Kernphysik, Johannes Gutenberg-Universität Mainz, 55128 Mainz, Germany*
[12]*Department of Physics, Engineering Physics, and Astronomy, Queen's University, Kingston, Ontario, K7L 3N6, Canada*
[13]*Royal Holloway University London, Egham Hill, Egham, Surrey TW20 0EX, United Kingdom*
[14]*Rutherford Appleton Laboratory, Harwell Oxford, Didcot OX11 0QX, United Kingdom*
[15]*SNOLAB, Lively, Ontario, P3Y 1M3, Canada*
[16]*University of Sussex, Sussex House, Brighton, East Sussex BN1 9RH, United Kingdom*
[17]*TRIUMF, Vancouver, British Columbia, V6T 2A3, Canada*

(Received 13 February 2019; published 24 July 2019)

DEAP-3600 is a single-phase liquid argon (LAr) direct-detection dark matter experiment, operating 2 km underground at SNOLAB (Sudbury, Canada). The detector consists of 3279 kg of LAr contained in a spherical acrylic vessel. This paper reports on the analysis of a 758 tonne · day exposure taken over a period of 231 live-days during the first year of operation. No candidate signal events are observed in the WIMP-search region of interest, which results in the leading limit on the WIMP-nucleon spin-independent cross section on a LAr target of 3.9×10^{-45} cm^2 (1.5×10^{-44} cm^2) for a 100 GeV/c^2 (1 TeV/c^2) WIMP mass at 90% C.L. In addition to a detailed background model, this analysis demonstrates the best pulse-shape discrimination in LAr at threshold, employs a Bayesian photoelectron-counting technique to improve the energy resolution and discrimination efficiency, and utilizes two position reconstruction algorithms based on the charge and photon detection time distributions observed in each photomultiplier tube.

DOI: 10.1103/PhysRevD.100.022004

[*]Deceased.
[†]Corresponding author.
deap-papers@snolab.ca

I. INTRODUCTION

An abundance of astrophysical observations indicates that dark matter, a nonluminous form of matter not described by the Standard Model of particle physics, comprises approximately 27% of the total energy density of the Universe [1]. By contrast, baryonic matter is estimated to account for 5% of the energy density. Despite the significant abundance, dark matter has not yet been directly detected in terrestrial experiments. Many theoretical models predict particles with appropriate phenomenological properties, such as those described in [2,3]. One such candidate is the weakly interacting massive particle (WIMP). In such models, the elastic scattering of WIMPs with nuclei produces low-energy ($\lesssim$100 keV) nuclear recoils (NRs) [4]. Direct detection experiments seek to observe this signature; current results limit the spin-independent WIMP-nucleon scattering cross section to be less than 9.0×10^{-47} cm^2 at 100 GeV/c^2 at 90% C.L. [5].

Detecting these rare, low-energy signals is facilitated by a large target mass with exceptionally low backgrounds, below 1 event per tonne per year. Previous experimental results demonstrated the effectiveness of liquid argon (LAr) for achieving these conditions [6,7]. Ease of purification, high scintillation efficiency and transparency to its own scintillation light makes it well suited for a multitonne WIMP detector. The DEAP-3600 experiment uses the unique scintillation time profile of LAr to achieve pulse shape discrimination (PSD) [8]. It has previously been shown that PSD can be used to suppress electronic recoil (ER) backgrounds by a factor better than 2.7×10^{-8}, in an energy range of 44–89 keV$_{ee}$ [9].

The results presented here are from the DEAP-3600 experiment, using nonblinded data collected from November 4, 2016 to October 31, 2017. DEAP-3600 has previously performed the first WIMP search with a single-phase LAr detector (measuring scintillation only), during a 14.8 tonne · day total exposure [6]. In this paper, the results are updated to a 758 tonne · day total exposure collected during 231 live-days. The result is the most sensitive dark matter search performed using a LAr target for WIMP masses above 30 GeV/c^2. This analysis shows the strongest background discrimination using PSD in any dark matter search, achieving an average leakage probability of $4.1^{+2.1}_{-1.0} \times 10^{-9}$ with 90% NR acceptance in the dark matter search region of 15.6–32.9 keV$_{ee}$.

II. DETECTOR AND DATA ACQUISITION

The DEAP-3600 detector is located approximately 2 km (6 km water-equivalent) underground at the SNOLAB facility near Sudbury, Ontario, Canada. In the current run, the detector has been operating with a LAr target since November 4, 2016. The analysis of data from a previous run is discussed in [6]. For the data collection period discussed here, the total mass of the LAr target is (3279 ± 96) kg. This value of the total LAr mass is calculated using the same method as described in [6].

A. Detector description

A cross-sectional diagram of the DEAP-3600 detector is shown in Fig. 1. The complete design of the detector is detailed in [10]. The detector consists of ultrapure LAr contained in a 5 cm thick ultraviolet absorbing (UVA) acrylic vessel (AV) with an inner diameter of 1.7 m. This UVA acrylic was chosen to reduce the amount of Cherenkov light originating from the acrylic. The top 30 cm of the AV is filled with gaseous argon (GAr). The GAr/LAr interface is 55 cm above the equator of the AV. The GAr and LAr regions are viewed by an array of 255 inward-facing 8″ diameter Hamamatsu R5912 HQE low radioactivity photomultiplier tubes (PMTs). The characterization of these PMTs is discussed in [11]. These PMTs are optically coupled to 45 cm long UVA acrylic

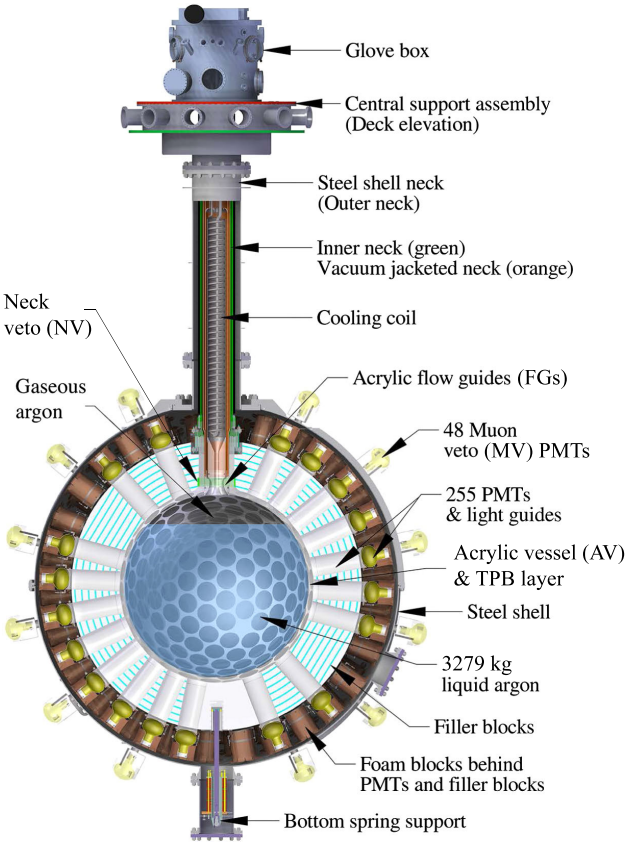

FIG. 1. Cross section of the DEAP-3600 detector components located inside the water tank (not shown). Inside the steel shell are inward-looking PMTs, light guides, filler blocks, and the AV, which holds the liquid argon target and the gaseous argon layer. Located on the outer surface of the steel shell are muon veto PMTs. Above this, a steel neck contains the neck of the AV, acrylic flow guides and the cooling coil. The neck is coupled to a central support assembly on which the glovebox is located. Shown also is the neck veto fiber system (green).

light guides (LGs), which transport visible photons from the AV to the PMTs. The volume between the LGs is filled with alternating layers of high density polyethylene and Styrofoam "filler blocks," which provide passive shielding of neutrons from detector components such as the PMTs. The filler blocks also provide thermal insulation so that the PMTs operate between 240 and 290 K.

The inner surface of the AV is coated with a 3 μm layer of 1,1,4,4-tetraphenyl-1,3-butadiene (TPB) that converts 128 nm scintillation light produced by the LAr to visible wavelengths over a spectrum that peaks at 420 nm [12]. The TPB was evaporated onto the inner surface of the AV using a spherical source that was lowered in through the AV neck; this process and characterization of the TPB coating is discussed in [13]. At the wavelengths emitted by the TPB, the light can travel through the AV and LGs and be detected by the PMTs, near their peak quantum efficiency. These LG-coupled PMTs provide 76% coverage of the AV surface area. There are 11 distinct "pentagonal" regions on the AV surface with reduced LG coverage that are each smaller in diameter than a LG. Excluding these pentagonal regions, the LGs are approximately uniformly spaced around the outer AV surface. The outer surfaces of the AV between LGs as well as the LGs themselves are, respectively, covered with diffuse Tyvek reflectors and Mylar to enhance light collection.

The spherical symmetry of the detector volume is broken by an opening at the top of the AV, which leads to a UVA acrylic neck and flange. This flange is connected to a longer stainless steel vacuum-jacketed neck ending in the glove-box. The neck contains a stainless steel liquid N_2-filled (LN_2) cooling coil, which condenses GAr during filling and operation. The condensed LAr enters the AV, directed by a set of UVA acrylic flow guides (FGs) located at the opening of the neck. These FGs direct the flow of argon to and from the cooling coil during detector operation.

Two bundles of uncladded Kuraray Y11 wavelength shifting optical fibers are wrapped around the base of the outer surface of the AV neck. Both ends of each bundle couple to a Hamamatsu R7600-300 PMT, for a total of 4 neck veto (NV) PMTs. They are located above the filler blocks that surround the AV neck at a distance from the AV center equal to the other AV PMTs. The NV is used to tag any visible light produced close to the AV neck, a relatively photon-insensitive region of the detector.

Prior to coating the AV with TPB and filling the detector, a mechanical resurfacer was lowered into the detector under a low-radon atmosphere in order to remove the inner 0.5 mm layer of acrylic along with ^{222}Rn progeny that either adsorbed to or diffused into the acrylic surface while it was exposed to air during construction [14].

The entire assembly as described is contained in a stainless steel sphere that is purged with a constant flow of Rn-scrubbed N_2 gas. This sphere is submerged in a 7.8 m high by 7.8 m diameter wide water tank with 48 outward-looking 8″ diameter Hamamatsu R1408 PMTs mounted on its outer surface. Together, these PMTs and the water tank constitute a Cherenkov muon veto (MV) used for tagging cosmogenically induced backgrounds, while the shielding water provides suppression of neutron and gamma backgrounds from the cavern.

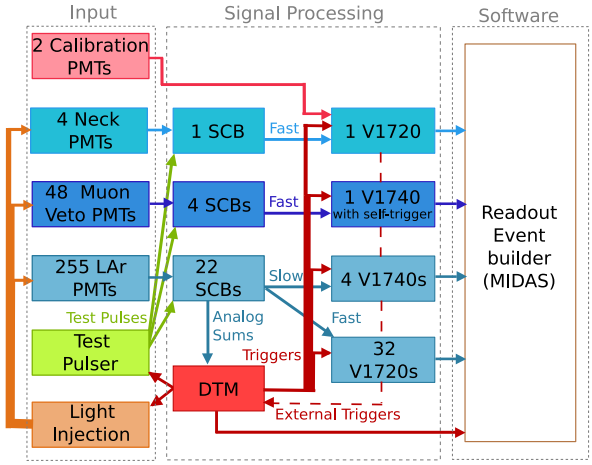

FIG. 2. A block diagram of the DEAP-3600 data acquisition system, adapted from [10]. Shown are the PMTs, the digitizer and trigger module (DTM), the signal conditioning boards (SCBs), the event builder, the light injection system, the test pulser systems, the fast high-gain channel digitizers (V1720s), and the slow low-gain channel digitizers (V1740s).

A series of calibration tubes are placed from the top of the MV at locations around the stainless steel sphere. These tubes allow radioactive sources to be lowered into the MV, at various locations around the outside of the detector, so that it may be calibrated with neutron and γ-ray sources. Calibration sources may be deployed with a set of detectors viewed by an additional pair of calibration PMTs, allowing tags to be generated for events in coincidence with a radioactive decay of the source.

B. Data acquisition

A block diagram of the data acquisition (DAQ) system is shown in Fig. 2. The DAQ is designed to digitize all signals from the inner detector PMTs in order to achieve a timing resolution of <1 ns. Each PMT is connected to one of 12 channels on a custom-built signal conditioning board (SCB). The SCBs decouple the signal from the high voltage and shape the signals to optimize digitization. A total of 27 SCBs are required for all of the AV, MV, and NV PMTs.

The SCBs output to both high-gain (V1720) and low-gain (V1740) waveform digitizer channels, which sample at 250 MS/s and 62.5 MS/s, respectively. Signals from the high-gain channels are used in most of the analysis, while those from low-gain channels extend the dynamic range of the detector for high-energy events, such as those generated by the α-decays of ^{222}Rn and ^{220}Rn progeny in the LAr target.

Each SCB sums all its inputs and provides that signal to a digitizer and trigger module (DTM), which determines when trigger conditions have been met. The DTM defines two rolling charge integrals: Q_n, a narrow integral over a 177 ns window, and Q_w, a wide integral over a 3.1 μs window. The DTM then computes Q_n/Q_w to estimate the prompt fraction of charge. Both Q_n and Q_n/Q_w are used by the DTM trigger decision algorithm. The DTM prescales 99% of ER-like signals ($Q_n/Q_w < 0.45$) in the energy range $Q_n \approx 50$–$565\,\mathrm{keV_{ee}}$ which is predominantly populated by ^{39}Ar decays. Only the DTM summary information is recorded for these events, including variables such as the trigger time, Q_n, and Q_w. For all other kinds of events, the trigger signal is sent to the digitizers. Special trigger signals can be set for calibration purposes.

When a trigger signal is received by the digitizers, PMT waveforms are recorded on each channel for a total length of 16 μs, with 2.4 μs before the trigger.

The 48 MV PMTs are independently read out by an additional V1740 digitizer operating in "self-trigger" mode.

Zero-length encoding (ZLE) is employed, along with other algorithms, to reduce the volume of data recorded to disk. This algorithm implements zero suppression in the firmware of each channel by ignoring regions of the waveform that are more than 80 ns removed from a per-channel voltage threshold, set to 10% of the mean amplitude of a single photoelectron (SPE). Individual PMT signals—such as photoelectrons (PEs)—are identified from these blocks of data.

The data acquisition system is discussed in more detail in [10].

C. PMT calibration

The following AV PMT characteristics were calibrated before the detector was filled with LAr: (1) the channel-to-channel PMT timing variation, which is constrained to <1 ns, (2) the relative channel efficiencies (CEs), which besides the PMTs' quantum efficiencies include the effect of attenuation in the LGs and LG-PMT couplings, and (3) the PMTs' afterpulsing (AP) rates and time distributions [10,11]. Since the LAr fill, the stability of the relative efficiencies and of the afterpulsing rates is monitored continuously, and the PMT single photoelectron (SPE) charge response is calibrated daily to within $\pm 0.3\%(\mathrm{stat})\ \pm 3\%(\mathrm{syst})$ [11]. The ongoing monitoring and calibration use both an LED light injection system [10,11] and the LAr scintillation light. The efficiencies and SPE charge response of the MV PMTs are also calibrated regularly using injected LED light.

The stability of the PMTs is discussed in more detail in Sec. VI. Further details on the PMT calibration and stability monitoring techniques are discussed in [11].

III. DATA PROCESSING AND RECONSTRUCTION

Data are recorded using MIDAS [15]. Data analysis and Monte Carlo simulations are performed using the RAT framework [16], based on ROOT [17] and GEANT4 [18].

Binary files produced by MIDAS are processed with RAT to produce a list of ZLE waveforms for each channel, with identified PE detection times in the corresponding PMT. These values are calibrated for channel timing offsets, time-of-flight, and PMT gains, and they are used to compute analysis variables, such as the energy estimator and PSD parameter described below.

A. Time-of-flight corrections

Because of its size and time resolution, DEAP-3600 is sensitive to the time-of-flight of photons from the scintillation vertex to the PMTs. To correct for this, an algorithm is employed to estimate the true event time and position. This algorithm considers a test position $\vec{x}_0$ and event time t_0. For each PE detected, the "time residual" t_{res} is calculated as the difference between the PE detection time and t_0 in excess of the time-of-flight implied by the straight-line distance from $\vec{x}_0$ to the relevant PMT. Values for $\vec{x}_0$ and t_0 are chosen to minimize $\sum t_{\mathrm{res}}^2$ for pulses with $t_{\mathrm{res}} < 8$ ns. The best fit value of t_0 is then subtracted from each PE detection time.

B. Photoelectron counting

A first order estimate of the number of PEs detected by a PMT can be found by integrating the observed charge and dividing by the mean SPE charge for that PMT. This method was used in the first DEAP-3600 result [6]. This technique is subject to two factors which degrade the energy resolution: the width of the SPE charge distribution and the presence of AP charges. Since PSD relies on measuring the number of prompt and late scintillation PEs, mitigating these uncertainties can improve PSD effectiveness. The root-mean-square (rms) of the SPE charge distribution is measured to be ~43% of the mean for the AV PMTs, using laser calibration data [11]. Similarly, the mean probability of a PE in an AV PMT generating an AP is measured to be $(7.6 \pm 1.9)\%$.

The PE measurement is improved by using a Bayesian PE-counting algorithm, which determines the most likely number of PEs in a PMT pulse, factoring out charge produced by APs [19,20]. This algorithm uses a prior distribution based on the number of PEs and APs preceding a pulse, given its charge, the LAr scintillation time profile, and the APs' time and charge distribution for the relevant PMT. The prior and the SPE charge distribution are used to compute the posterior distribution of the number of PEs. Instead of using the most likely number of PEs in a pulse, as described by [20], the mean of the posterior distribution is used, as it was found to more accurately reproduce the tail of the pulse shape [21].

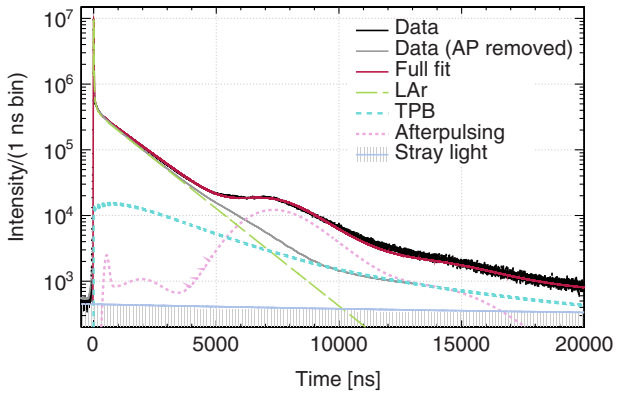

FIG. 3. Average ^{39}Ar pulse shape before correction of instrumental effects (black) shown together with a model fit (red). The fit accounts for the following effects, which are shown individually: LAr singlet, triplet, and intermediate [23] light emission (green dashed), TPB prompt and delayed light emission [24] (blue dash-dotted), afterpulsing following all the previous components (pink dotted), and stray light (grey filled), which accounts for dark noise and the delayed TPB emission from previous events. The pulse shape made from pulses that use the pulse-by-pulse AP removal algorithm (see text) is also shown (grey solid).

This algorithm is applied to each SPE-calibrated PMT signal and is summed over all such signals in the first 10 μs of an event to determine the expected number of PEs. The specific implementation of this algorithm and a description of its effects on PSD are discussed separately in more detail in [21,22]. Figure 3 illustrates how this algorithm separates PEs and AP charges, on average. After AP removal, the pulse shape can be seen to closely follow the LAr scintillation and TPB fluorescence time profiles.

C. PSD parameter

The parameter F_{prompt} is defined as the fraction of PE detected in a prompt window around the event time. The maximum separation between ER and NR events was obtained with a prompt window spanning $[-28, 60]$ ns around the event time. F_{prompt} is therefore calculated by

$$F_{prompt} = \frac{\sum_{t=-28\ ns}^{60\ ns} PE(t)}{\sum_{t=-28\ ns}^{10\ \mu s} PE(t)}. \quad (1)$$

IV. DETECTOR RESPONSE CALIBRATION

The light yield, energy resolution, and F_{prompt} distributions are calibrated using external radioactive sources lowered into one of the calibration pipes running along the outside of the stainless steel sphere, or using internal radioactivity naturally present in the detector, such as ^{39}Ar. Monoenergetic gamma lines are used as a cross-check.

A. Light yield and energy resolution

The detector energy response is calibrated using the ER events generated by the β-decays of the trace ^{39}Ar isotope in the LAr target. The calibration is compared to measurements with a ^{22}Na source and naturally occurring γ-ray lines from detector materials. Note that ^{39}Ar is naturally present in atmospherically derived LAr and β-decays with a half-life of 269 yr and an endpoint of (565 ± 5) keV [25]. It has been measured to have a specific activity of (0.95 ± 0.05) Bq/kg [26].

A parametrization of the ^{39}Ar spectrum to ER data describes a response function that relates the energy deposited in the detector, E, to the number of detected PEs. It assumes a Gaussian response with mean μ and variance σ defined as follows,

$$\mu = \langle N_{DN} \rangle + Y_{PE} \cdot E,$$
$$\sigma^2 = \sigma^2_{PE} \cdot \mu + \sigma^2_{rel,LY} \cdot \mu^2, \quad (2)$$

where $\langle N_{DN} \rangle$ is the average number of PEs produced by dark noise and uncorrelated photons in the PE integration window, Y_{PE} is the light yield of the detector, σ^2_{PE} is a resolution scaling factor that accounts for effects such as the Fano factor and PE counting noise, and $\sigma^2_{rel,LY}$ accounts for the variance of the light yield relative to its mean value.

Note that Y_{PE}, σ^2_{PE}, and $\sigma^2_{rel,LY}$ are treated as fit parameters, and $\langle N_{DN} \rangle$ is constrained by looking at PMT signals preceding scintillation events. When performing spectral fits, $\langle N_{DN} \rangle$ is allowed to float, while a penalty term maintains that it stay within the uncertainty of its nominal value. The value of $\langle N_{DN} \rangle$ is found to be (1.1 ± 0.2) PE in standard physics runs. For data taken with a ^{22}Na source, it is measured to be (2.1 ± 0.2) PE. Note that $\langle N_{DN} \rangle$ is higher when a calibration source is present due to the higher scintillation rate during these runs producing uncorrelated background photons from slow TPB fluorescence on millisecond timescales [24].

The ^{39}Ar β-decay spectrum used in this analysis was calculated in [27], in which the shape factor is computed using nuclear shell model and microscopic quasiparticle-phonon model codes. This spectrum was fit to the observed PE distribution, with additional contributions from ^{39}Ar pileup events and γ-ray backgrounds, generated by Monte Carlo simulations. The γ-ray spectrum is normalized to the observed rates of events coming from decays of ^{40}K, ^{214}Bi, and ^{208}Tl seen at higher energies.

Uncertainties in the spectral shape of the ^{39}Ar energy spectrum were probed by fitting spectra evaluated from [28–30] to the data. These calculations approximate the shape factor following the prescription in [28] while making additional finite nuclear size and mass corrections and radiative corrections. The best fit was obtained using the spectrum from Kostensalo *et al.* [27], which converged with $\chi^2/\mathrm{NDF} = 1252/534$ in the 80–4500 PE range.

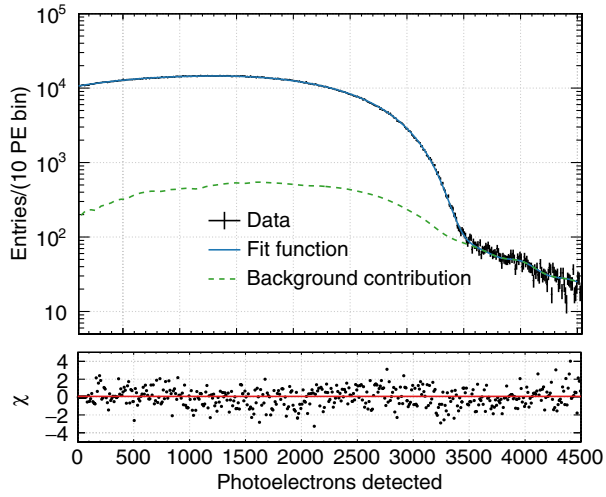

FIG. 4. The ^{39}Ar model (blue line) fit to data (black). Included in the fit is the expected background contribution from γ-rays and ^{39}Ar pileup events (green).

Further studies to better understand the ^{39}Ar spectral shape are currently planned. These efforts include studying the effects of additional nuclear effects such as weak magnetism, as alluded to in [30], and applying additional radiative corrections to the spectrum computed in [27].

To account for potential mismodeling uncertainty, additional fits were performed, allowing for first-order corrections to the ^{39}Ar spectrum $S_{\mathrm{Ar}}(E)$ with a slope treated as a nuisance parameter a_0. An additional penalty term of $(a_0/0.01)^2$ was added to χ^2, to constrain its value close to 0. The modified β-spectrum is described by

$$S'_{\mathrm{Ar}}(E) = (1 - a_0(1 - 2E/500))S_{\mathrm{Ar}}(E), \qquad (3)$$

where E is the energy of the β particle in units of keV. While such excursions may be due to deviations in the ^{39}Ar spectrum from the tested models, further studies are needed before a physical interpretation can be assigned to the value of a_0.

With this nuisance parameter, the fit was found to converge with $\chi^2/\mathrm{NDF} \approx 542/433$, with a 7%–9% deviation from the spectrum derived in [27]. The origin of this deviation is not yet understood and is still being investigated. It is found to have little effect on the best fit values of the response function parameters or on the final WIMP search result. The results of this fit are shown in Fig. 4. The differences between the best fit values for each parameter with and without the nuisance parameter are propagated into the parameters' uncertainties. The best fit response function parameters are shown in Table I.

A ^{22}Na source was lowered into the calibration tubes outside the stainless steel shell to compare the consistency of the response function calibrated with ^{39}Ar to the spectrum produced by events from tagged ^{22}Na decays, which contains a prominent 1.27 MeV γ-ray and a low-energy spectrum feature resulting from γ-rays attenuating in acrylic [6]. A cross-check using the γ-ray lines from ^{40}K (1.46 MeV), ^{214}Bi (1.76 MeV), and ^{208}Tl (2.61 MeV) is also performed. These isotopes are naturally present in detector materials and are visible in standard physics runs. Figure 5 shows the estimated number of detected PEs using the light yield from ^{39}Ar extrapolated out to these energies. As shown in this figure, the energy response function remains very linear over a wide range of energies, with nonlinearities starting to arise above 1.46 MeV due to digitizer saturation.

TABLE I. Best fit response function parameters from a fit to ^{39}Ar events collected throughout the data collection period. The fit converged with χ^2/NDF of 542/433. The value shown for $\langle N_{\mathrm{DN}} \rangle$ is derived from direct measurements, as described in the text.

PE mean	$\langle N_{\mathrm{DN}} \rangle$	Y_{PE}
	(1.1 ± 0.2) PE	(6.1 ± 0.4) PE/keV$_{\mathrm{ee}}$
Resolution	σ^2_{PE}	$\sigma^2_{\mathrm{rel,LY}}$
	(1.4 ± 0.1) PE	$0.0004^{+0.0010}_{-0.0004}$

Data were also collected with an AmBe neutron source deployed in order to validate the NR quenching and PSD models. NR quenching factors were derived from SCENE measurements [31], using the Lindhard-Birks model fit to the measured NR light yields relative to ^{83m}Kr ERs. The estimated uncertainties for these quenching factors were dominated by the uncertainty in the Birks factor.

This model is implemented in the simulation and validated by comparing the observed PE spectrum of neutron-induced NRs in the AmBe neutron source data to the simulated one. The agreement between the model and data can be seen in Fig. 6.

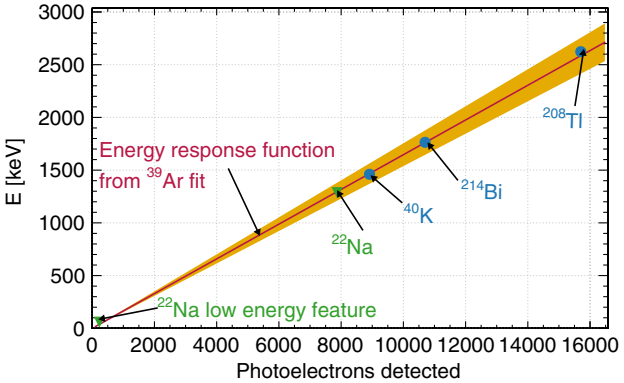

FIG. 5. The energy response function (red), showing the number of detected PE for an event depositing energy E in the LAr. The uncertainties of the response function are also shown (yellow band). The response function agrees with the number of PE detected from known monoenergetic sources of γ-rays from the detector materials.

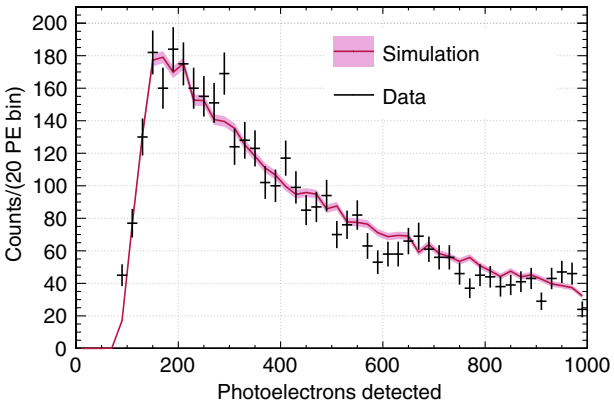

FIG. 6. Comparison of the detected PE distribution for high-F_{prompt} NR-like events from an AmBe neutron source simulation (pink) and data (black). The peak at low PE is due to the F_{prompt} cut that removed ERs; due to the high rate of ERs in coincidence with neutron-induced NRs in the calibration data, particularly strong cuts are needed to obtain a clean NR spectrum. Uncertainties shown are all statistical, using nominal values for the quenching and detector optics models.

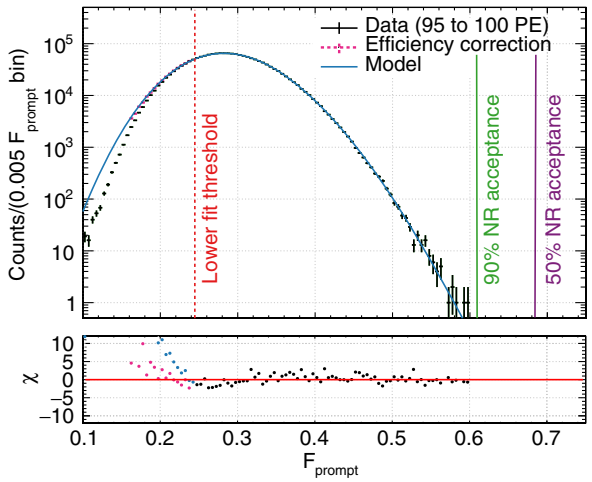

FIG. 7. F_{prompt} distribution for ERs from standard physics data in the lowest 1 keV_{ee} energy bin in the WIMP-search region of interest. The PSD model is fit to the data to the right of the vertical dashed line, where the trigger efficiency is approximately unity. Agreement between the best fit model and the data can be seen; below the F_{prompt} fit region, trigger efficiency corrections to the data show that the model agrees when extrapolated to lower values. Solid vertical lines show the F_{prompt} value in the corresponding PE bins above which 90% or 50% of NRs are expected to be found. In the bottom plot, black points show residuals over the range where the model is fit; blue points compare the extrapolated model directly to the observed data prior to correcting for the decreasing trigger efficiency, while pink points compare the extrapolated model to the data after making these corrections.

B. F_{prompt} distributions

Following a particle interaction, excimers form in the LAr, and the singlet/triplet population ratio is a function of the nature and the energy of the interaction. Due to the different decay times of the two types of excimers, different particles produce different F_{prompt} distributions that vary with their energy. In this analysis, PSD is used to differentiate between NRs, ERs, and α particle interactions.

1. Electronic recoils

An empirical function has been developed that characterizes the F_{prompt} distribution for ERs; this function was chosen as it was found to describe the data well over a wide range of energy. For an ER event in which q PE are detected, the probability of observing an F_{prompt} value of f is described by

$$\begin{aligned} F^{\mathrm{ER}}(f,q) &= \Gamma(f;\bar{f},b) * \mathrm{Gauss}(f;\sigma), \\ \bar{f}(q) &= a_0 + \frac{a_1}{q-a_2} + \frac{a_3}{(q-a_4)^2}, \\ b(q) &= a_5 + \frac{a_6}{q} + \frac{a_7}{q^2}, \\ \sigma(q) &= a_8 + \frac{a_9}{q} + \frac{a_{10}}{q^2}, \end{aligned} \tag{4}$$

where $\Gamma(f;\bar{f},b)$ is the Gamma distribution with mean $\bar{f}$ and shape parameter b, and $\mathrm{Gauss}(f,\sigma)$ is a Gaussian distribution with standard deviation σ and a mean of 0. The parameters a_i are fit parameters that describe how $\bar{f}$, b, and σ vary with q.

The parameters a_i are fit to the distribution of F_{prompt} vs PE. Within each PE bin, the resulting values of $\bar{f}$, b, and σ describe the shape of the F_{prompt} distribution, neglecting trigger efficiency effects. In each PE bin, the fit considers values of F_{prompt} for which the trigger efficiency is estimated to be greater than 99.95%. The resulting fit is well constrained and converges with $\chi^2/\mathrm{NDF} = 14,329/9380$. In effect, $\bar{f}$, b, and σ are the physically relevant parameters, while a_i parametrize their energy dependence, forcing them to vary smoothly across PE bins and allowing F_{prompt} distributions to be interpolated. An example of this fit in a single PE bin is shown in Fig. 7. The validity of this fit has been tested by performing it over a limited range of F_{prompt} and comparing extrapolated values to the data outside the fit range. These tests show that extrapolated expectations agree with the data, indicating the robustness of this method.

Since the DTM triggers on the number of prompt PEs, low F_{prompt} events at low PE are less likely to produce a trigger signal. A software correction has been developed to account for the reduced trigger efficiency for these events, following the procedure described in [32]. Data with this correction applied are shown in Fig. 7. While $F^{\mathrm{ER}}(f,q)$ is only fit over the range where the trigger efficiency is near unity, the extrapolated model agrees better with the efficiency-corrected F_{prompt} distribution.

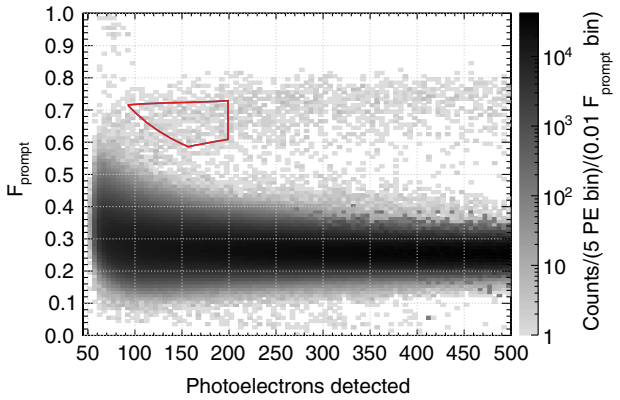

FIG. 8. F_{prompt} vs PE distribution for data taken with an AmBe neutron source near the equator of the stainless steel shell. The WIMP-search ROI is shown in red. Separation can be seen between the NR band ($F_{prompt} \sim 0.7$) and ER band ($F_{prompt} \sim 0.3$). Events in the prescaled region (ER band with PE $\gtrsim 300$) are weighted with a correction factor of 100, corresponding to the prescale factor. Note that multiple neutron scatters and pileup with Cherenkov and ER signals bias the NR spectrum away from the expected distribution for pure single-scatter NRs and populate the region between both bands.

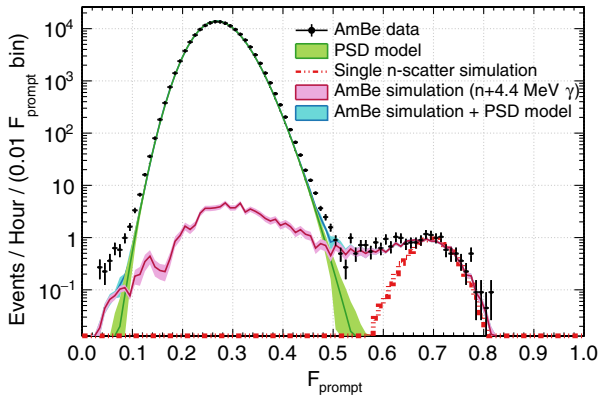

FIG. 9. F_{prompt} distribution in the 120–200 PE range of events from AmBe data (black) and simulations of single-scatter neutrons (red dashed). Also shown are simulated events from an AmBe source (pink), the ER PSD model (green) and their sum (blue).

2. Nuclear recoils

Mean F_{prompt} values for NRs are determined from measurements reported by the SCENE Collaboration [31]. SCENE reports median values of F_{90}, defined as the fraction of charge observed in the first 90 ns of an event, for different NR energies. Equivalent singlet/triplet ratios are determined for each median F_{90} value, which are used as input to a Monte Carlo simulation of DEAP-3600. This simulation propagates the detector timing response, including photon times-of-flight and PMT effects such as AP into the resulting F_{prompt} distribution. Uncertainties in the extracted singlet/triplet ratio are determined from uncertainties reported by SCENE as well as uncertainties in the singlet and triplet lifetimes. Uncertainties from the AP rates and triplet lifetime in DEAP-3600 are also propagated into the uncertainty on the mean F_{prompt} values.

For NRs, it is assumed that the spread of the F_{prompt} distribution around the mean is governed by the same effects that drive the spread in the ER distribution, with an inverted skew. The F_{prompt} distribution for NRs with q PE is then given by

$$\begin{aligned} F^{\mathrm{NR}}(f,q) &= \Gamma(1-f;1-\bar{f},b) * \mathrm{Gauss}(f;\sigma), \\ b(q) &= a_5 + \frac{a_6}{q} + \frac{a_7}{q^2}, \\ \sigma(q) &= a_8 + \frac{a_9}{q} + \frac{a_{10}}{q^2}, \end{aligned} \tag{5}$$

where $\bar{f}(q)$ is the mean F_{prompt} value for NRs at q, predicted by the simulation, and $b(q)$ and $\sigma(q)$ are governed by the fit parameters a_i in Eq. (4).

The NR F_{prompt} distribution is validated using AmBe calibration data. An AmBe neutron source was lowered into a calibration tube outside of the stainless steel shell of the detector. The resulting signal seen in the detector is shown in Fig. 8, with the WIMP-search ROI shown for comparison. Many of the neutron-induced NRs are accompanied by ER or Cherenkov pileup from γ-rays correlated with neutron production in the AmBe source, while others are biased by multiple scatter events. As a result, we do not expect the AmBe data to directly reproduce the F_{prompt} distribution predicted for single scatter NRs. Instead, we simulate the AmBe source and compare the simulated and observed F_{prompt} distributions. Figure 9 shows this comparison; agreement between data and simulation to within uncertainties indicates the validity of the model.

3. α decays

DEAP-3600 detects full energy α-decay events produced by ^{222}Rn, ^{220}Rn, and their progeny from within the LAr. These events reconstruct above ~23000 PE and are subject to digitizer and PMT saturation effects that reduce the number of detected PE and the value of F_{prompt} when using the normal high-gain scheme intended for low PE events. This effect broadens PE and F_{prompt} distributions, biasing their values downward by preferentially causing the number of prompt PE to be underestimated.

The three most frequent α-decays in the LAr are ^{222}Rn, ^{218}Po and ^{214}Po (α-particle energies of 5.5 MeV, 6.0 MeV, and 7.7 MeV, respectively). Signals observed using the low-gain channels are used to apply digitizer and PMT saturation corrections to signals observed in the high-gain channels, as described in [33]. These corrections allow for more accurate F_{prompt} and PE values to be calculated and a parametrization between the mean F_{prompt} as a function of α-particle energy. This parametrization is implemented into

the simulation for α-particle scintillation in LAr, and extrapolated across the energy range 5.0–10.0 MeV such that ^{210}Po (5.3 MeV) and higher energy ^{220}Rn daughters like ^{212}Po (8.8 MeV) can be modeled. At 5.3 MeV, the model uncertainty corresponds to a 3.5% uncertainty in the mean F_{prompt} value.

Understanding the relationship between the mean F_{prompt} and energy for α particles allows for modeling of high-energy α-decays in the AV neck region. These events are shadowed and reconstruct with low PE. As will be discussed in Sec. VII D 3, such events are caused by the absorption of ultraviolet (UV) scintillation by acrylic components in the AV neck. These events are not affected by digitizer clipping or PMT saturation effects, and hence the F_{prompt} of these events preserves information about the α-particle energy that produced them.

V. POSITION RECONSTRUCTION

DEAP-3600 utilizes two complementary position reconstruction algorithms: one using the spatial distribution of PMT hits (PE-based algorithm) and one that also includes timing information (time residual-based algorithm).

The PE-based algorithm computes the likelihood $\mathcal{L}(\vec{x})$ that the scintillation event happened at some test position $\vec{x}$ as

$$\begin{aligned} \ln \mathcal{L}(\vec{x}) &= \textstyle\sum_{i=1}^{N_{\mathrm{PMTs}}} \ln \mathrm{Poisson}(q_i;\lambda_i), \\ \lambda_i &= \lambda_i\left(|\vec{x}|, \tfrac{\vec{x}\cdot\vec{r}_i}{|\vec{x}||\vec{r}_i|}, q_{\mathrm{total}}\right), \end{aligned} \tag{6}$$

where $\mathrm{Poisson}(q_i;\lambda_i)$ is the Poisson probability of observing q_i PE in PMT i at position $\vec{r}_i$ over the full 10 μs event window. The expected number of PE in PMT i is given by λ_i, which is a function of the radius of the test position $|\vec{x}|$, the angle between the test position and PMT_i, and total PE integrated over all PMTs q_{total}.

Values for λ_i are calculated based on a Monte Carlo simulation of the detector, including the full optical model. These simulations assume a completely filled detector, with scintillation events generated inside the LAr along three distinct axes: one collinear with the axis of the AV neck and two perpendicular axes within the equatorial plane of the AV. A set of splines is then used to generate tables of λ_i values. This algorithm does not account for timing information within the 10 μs event window. The position returned by this algorithm is the one that maximizes $\ln \mathcal{L}(\vec{x})$.

In contrast, the time residual-based algorithm uses both charge and time information of early pulses in an event to calculate the position. As with the time-of-flight corrections used to correct PE detection times, time residuals are defined as the time at which a PE was detected in excess of what the time-of-flight would suggest. However, this algorithm uses a more precise, albeit slower method for determining the time residuals. Prior to data processing, a grid of test positions $\vec{x}_j$ is defined inside the LAr relative to the PMT location, and the time residual distribution $\mathcal{L}^{t\mathrm{res}}(\Delta t;\vec{x}_j,\mathrm{PMT}_i)$ is calculated. These calculations utilize a simplified optical model of the detector, including the group velocities of UV photons emitted by LAr (11 cm/ns at 128 nm) and visible photons emitted by TPB (24 cm/ns at 420 nm), as well as the LAr scintillation and TPB fluorescence time constants, the average travel time of visible photons in the LG and AV acrylic, and the average PMT response time. The group velocities used for these calculations were determined based on measured LAr refractive indices at various wavelengths, as reported by [34], following the procedure described in [35].

In the simplified optical model, reflections and scattering of visible photons in TPB are neglected. Rayleigh scattering in the LAr is neglected as well; in the PE-based algorithm, scattering lengths of 1.65 m and 1082 m are assumed for wavelengths of 128 nm and 420 nm, respectively, following the procedure outlined in [35]. The time response of the LGs and PMTs from the initial calibration of the detector as discussed in Sec. II C is assumed.

The likelihood $\mathcal{L}(t_0,\vec{x}_0)$ of a given event time t_0 and test position $\vec{x}_0$ is computed as

$$\ln \mathcal{L}(t_0,\vec{x}_0) = \sum_{i=1}^{N_{\mathrm{PE}}} \ln \mathcal{L}^{t\,\mathrm{res}}(t_i - t_0;\vec{x}_0,\mathrm{PMT}_i), \tag{7}$$

where t_i is the time at which the ith PE was detected in channel PMT_i; the N_{PE} in the first 40 ns are considered for this calculation. This algorithm returns the values of $\vec{x}_0$ and t_0 that maximize $\ln \mathcal{L}(t_0,\vec{x}_0)$.

A. Validation

The WIMP-search analysis presented here relies primarily on the PE-based algorithm for fiducialization, though it also requires that both algorithms converge and agree with each other. Doing so allows for the rejection of events whose positions are misreconstructed, as may be the case for events originating outside of the LAr, where the assumptions underlying both algorithms are not realized.

Both algorithms are validated using ^{39}Ar β-decays, uniformly distributed in the LAr. Nonuniformities in their reconstructed positions therefore provide a measure of the algorithms' bias. Figure 10 demonstrates the uniformity of the PE-based algorithm. The time residual-based algorithm, which provides an additional test for misreconstruction, exhibits a sharp change between reconstructed radii values 350–400 mm. This nonuniformity is an artifact of the time-residual calculations used by this algorithm and is subject to refinement in a future analysis. The fiducial radius used in this analysis is 630 mm based on the returned value of the PE-based algorithm; at this value data and simulation agree to within 13%.

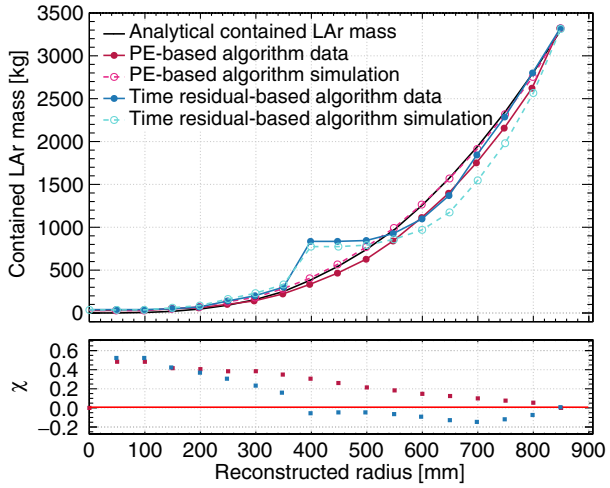

FIG. 10. Estimates from the PE-based (red) and time residual-based (blue) algorithms of the contained mass of LAr within a radius of the reconstructed position. The estimate is based on the total fraction of ^{39}Ar ER signals in the 95–200 PE range reconstructing within a given radius. Values from both data (solid) or simulations (dashed) are shown. It is assumed that the true positions of the ^{39}Ar nuclei are uniformly distributed throughout the LAr target. Shown also is the estimated contained mass calculated by considering only the geometric volume (black). The bottom inset shows the difference between data and simulation for each algorithm.

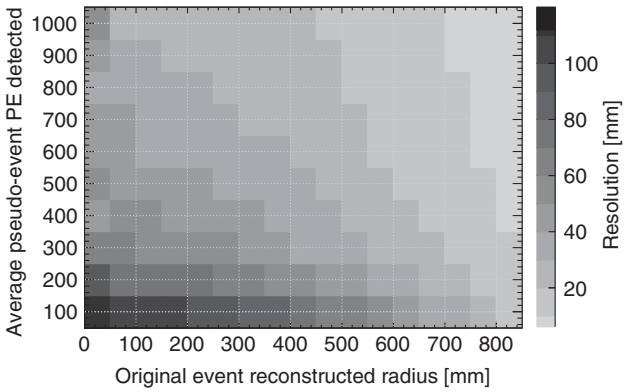

FIG. 11. Position resolution evaluated using the data-driven pseudoevent method, as a function of the average number of PE in both pseudoevents and the reconstructed radius drawn from the same original event, as returned by the PE-based algorithm. The z-axis scale denotes the resolution, defined as the characteristic width of the distribution of distances between reconstructed pseudoevents drawn from the same original event.

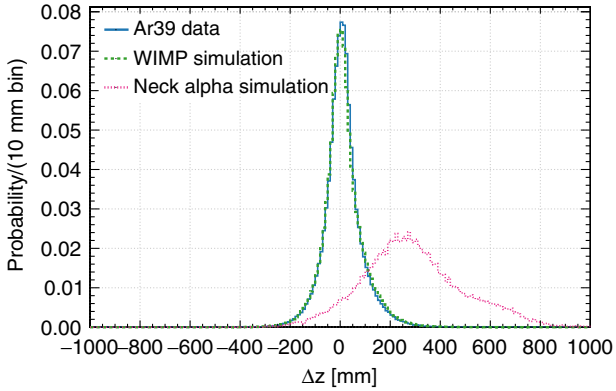

FIG. 12. The z-coordinate of the reconstructed position (along the axis parallel to the AV neck) as estimated by the time residual-based algorithm minus the z-coordinate estimated by the PE-based algorithm. Note that ^{39}Ar data (solid blue) and a simulation of WIMP NRs (dashed green) show similar distributions, centered around the origin. A significant offset is seen for simulated α-decays in the neck (dotted magenta).

A data-driven method is used to estimate the position resolution. First, ^{39}Ar β-decay events are split into two "pseudoevents": each PE from an event is independently assigned to each of the two pseudoevents with a 50% probability. Doing so results in both pseudoevents having approximately half the number of PEs as the original event, from the same true position. The position resolution is determined from the distribution of reconstructed distances between pseudoevents, in bins of average pseudoevent PE and original event reconstructed radius; the characteristic width of each such distribution is shown in Fig. 11. Within the WIMP-search PE region, near the 630 mm radial cut used in this analysis, pseudoevents typically reconstruct within 30–45 mm of each other.

Figure 12 shows the difference between the z-coordinates reconstructed by both algorithms, where the z-axis runs parallel to the AV neck. Both algorithms typically agree for ^{39}Ar events in data and for simulations of ^{40}Ar recoils, returning z-coordinates that agree to within 35 mm for 50% of such events. For simulated events generated by α-decays through a LAr film on the surface of the AV neck (to be discussed in Sec. VII D 3), this distribution is very different. The neck directs light to the bottom of the detector, causing the PE-based algorithm to reconstruct it with a low z-coordinate, while the time residual-based algorithm systematically reconstructs these events closer to the top of the detector. As a result, the time residual-based algorithm reconstructs these events an average of 290 mm higher than the PE-based algorithm. A similar shift is observed for neck α-decays when comparing the distance between reconstructed positions.

VI. DETECTOR STABILITY AND RUN SELECTION

The state of the DAQ and process systems is continuously monitored, and the quality of the data is assessed during collection and after processing. This allows for different levels of data quality checks. Data from the detector and from the DAQ and process system sensors are continuously monitored by automated processes and by the person on shift. Any anomalous behavior is flagged.

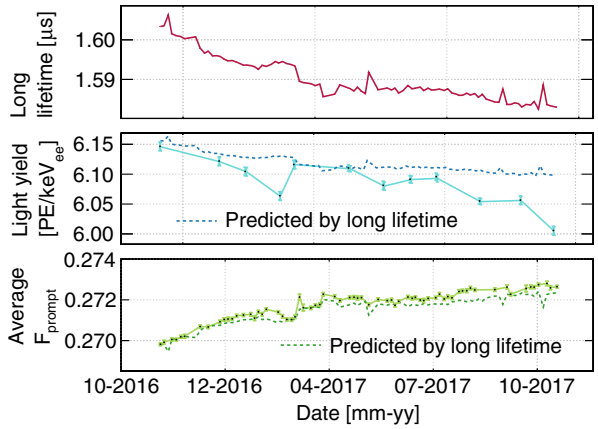

FIG. 13. Shown over the time period spanned by this data set is the long lifetime component of LAr scintillation (top), the detector light yield (middle), and mean F_{prompt} of ER signals generated by 2.61 MeV γ-rays in the LAr target throughout the run. For the latter two plots, the predicted value based on the long lifetime value at that time is also shown (dashed).

These data include, but are not limited to, PMT rates, PMT bias voltages, PMT baselines, AV pressure, and DAQ rack temperature.

For the data set discussed here, the LAr is not recirculated. Hence, the primary function of the process system is to maintain the LAr target inside the AV at a constant temperature and pressure. This is achieved through continuous circulation of LN_2 in the cooling coil. For further details on the process system, see [10].

Impurities (e.g., O_2, N_2) can decrease the scintillation yield [36–38] of LAr by absorbing the scintillation light and, for electronegative impurities, by capturing the excitation energy from the Ar excimers. Electronegative impurities thus preferentially suppress the triplet scintillation component and affect the PSD distributions [39,40].

The purity of the LAr target, and thus the stability of analysis inputs, is monitored by examining calibrated PMT waveforms from ^{39}Ar ER events and other detector backgrounds. This yields the LAr long lifetime component (which includes detector effects such as the slow component of the TPB response, as described in [24], and is not a direct measure of the decay constant of the triplet state of the Ar dimer) and the light yield at a granularity of better than 1 h. In the same processing step, self-diagnostic pulses injected into the data stream by the DAQ system are evaluated to verify proper behavior of each PMT channel. Any anomalous behavior is again flagged.

As shown in Fig. 13, throughout the time period discussed, the long lifetime and light yield were stable to within $\pm 1.0\%$ and $\pm 1.3\%$, respectively. The high value of the long lifetime shown here is indicative of a high level of chemical purity with regard to electronegative contaminants, in accordance with the design goals as described in [10]. The mean of the F_{prompt} distribution at high energies is directly affected by changes to the long lifetime component of LAr scintillation. The variation of F_{prompt} from high-energy ER events is shown also and is found to be stable to within $\pm 0.7\%$. Given this level of stability, no corrections are applied to account for temporal variations in the light yield or long lifetime. The dashed lines in Fig. 13 show what the light yield and mean F_{prompt} values would be if the decrease in the long lifetime was the only factor reducing their values.

Changes in the PMT response over the data taking period are accounted for in this analysis. For 250 of the 255 AV PMTs, the CEs are constant to within 1%. Two PMTs have changes of less than 10%. Three have changes in excess of 30%. One of the three is stable for the first two-thirds of the data collection period, after which it is removed from the analysis and omitted from calculations of analysis variables. The two remaining PMTs with large changes in CE are located about the pentagonal region at the bottom of the AV. Position reconstruction is particularly sensitive to changes in CE, as it relies on signals measured in individual PMTs.

The gain of each PMT is measured in the form of the mean SPE charge. The mean SPE charge, averaged over the 254 PMTs used throughout the entire data collection, is 1.043 times larger at the end of the data collection than at the beginning. The rms of this mean SPE charge ratio is 3.3%. These changes are also propagated through the analysis. The probability of afterpulsing is found to be stable to within $\pm 6\%$ of the quoted value and is fixed in the analysis throughout the data collection.

The 4 neck veto PMTs remained operational throughout the time period of this data set. In the MV, 45 PMTs remained stable and 3 failed.

A. Run selection and live time determination

Selection criteria are applied to each run to remove periods where instabilities could affect the dark matter search. These criteria include the stability of the AV cooling system, stability of the PMT charge distributions, and the trigger efficiency.

The first requirement is that the difference between the maximum and minimum values of the AV pressure recorded for the run corresponds to less than a 10 mm variation in the LAr fill level. Such variations are expected if maintenance is performed on the process system or when replenishing the LN_2 in circulation. The second requirement is based on the charge readout of each PMT channel, taken in 5 minute samples. Runs are omitted if at least one PMT exhibits intermittent behavior, defined as reading less than 50% of its nominal average charge at any stage throughout the run. While such excursions are rare and only occur in certain PMTs, they indicate temporary malfunctioning behavior in the corresponding PMTs. Finally, to maintain good calibration of the PSD model and its prediction throughout the data set, the last requirement is enforced based on whether the trigger efficiency

TABLE II. The cumulative impact of the run selection criteria on the data live time is shown. Below this, total fiducial LAr mass is shown after applying each fiducial cut cumulatively.

	Selection criteria	Live time [days]
Run	Physics runs	279.78
	Pass automatic DAQ & shifter checks	264.93
	Stable cryocooler	247.12
	Stable PMTs	246.91
	Trigger efficiency obtained	246.64
Event	Muon veto events	246.24
	Dead time	230.63
	Total	230.63

	Fiducial cut	Contained LAr mass [kg]
	No fiducial cuts	3279 ± 96
	Reconstructed position $z < 550$ mm & radius < 630 mm	1248 ± 40
	Charge fraction in top 2 rows of PMTs	921 ± 28
	Charge fraction in bottom 3 rows of PMTs	824 ± 25
	Total	824 ± 25

can be determined for the run. Due to drifts in the PMT gain and the details of how the DTM receives PMT signals, the trigger efficiency can vary slightly from run to run. The trigger efficiency is determined for each run using the method described in [32]. This procedure requires a large enough data sample in regions with low trigger efficiency. Runs that are shorter than approximately 1 h do not have enough statistics and are omitted. The point corresponding to 50% trigger efficiency varies by 10% between runs; these variations primarily affect ER events and are negligible for NRs in the ROI. These run selection criteria and their impact on the total live time are summarized as "Stable cryocooler," "Stable PMTs," and "Trigger efficiency obtained" in Table II, resulting in a live time loss of 6.9% after automatic DAQ and shifter checks.

The total live time is also affected by events in the MV passing the veto threshold ("Muon veto events") and by DAQ self-diagnostic triggers, the removal of pileup with ^{39}Ar, and Cherenkov events in the LGs. When an event passes the veto threshold of the MV, all AV events within a $[-0.1, 1]$ s window around the trigger are vetoed; noise and γ-rays causing the MV to pass the vetoing threshold therefore reduce the total live time. The three latter conditions are low-level cuts factored into the "Dead time" entry of Table II, resulting in a live time loss of 6.5% after applying run selection criteria. Cherenkov events generated in the LGs are one of two Cherenkov populations discussed in Sec. VII B 2. They are readily removed without affecting the WIMP acceptance and hence are factored into the dead time.

VII. BACKGROUND MODEL AND CUT SELECTION

WIMP-like events may be produced in the detector by a variety of background sources that include β particle and γ-ray interactions in the LAr and acrylic, neutron-induced nuclear recoils in the LAr, and α-decays from surfaces in contact with LAr. In this analysis, the total number of predicted background events after applying all event selection cuts in the WIMP search region of interest (ROI), $N_{\mathrm{bkg}}^{\mathrm{ROI}}$, is expressed as follows,

$$N_{\mathrm{bkg}}^{\mathrm{ROI}} = N_{\mathrm{ER}}^{\mathrm{ROI}} + N_{\mathrm{Cher}}^{\mathrm{ROI}} + N_{n,\mathrm{rdg}}^{\mathrm{ROI}} + N_{n,\mathrm{csg}}^{\mathrm{ROI}} + N_{\alpha,\mathrm{AV}}^{\mathrm{ROI}} + N_{\alpha,\mathrm{neck}}^{\mathrm{ROI}}, \tag{8}$$

where the individual terms are the expected number of background events from ERs ($N_{\mathrm{ER}}^{\mathrm{ROI}}$), Cherenkov light produced in acrylic ($N_{\mathrm{Cher}}^{\mathrm{ROI}}$), radiogenic neutrons ($N_{n,\mathrm{rdg}}^{\mathrm{ROI}}$), cosmogenic neutrons ($N_{n,\mathrm{csg}}^{\mathrm{ROI}}$), and α-decays from both the AV surface ($N_{\alpha,\mathrm{AV}}^{\mathrm{ROI}}$) and the AV neck flow guides ($N_{\alpha,\mathrm{neck}}^{\mathrm{ROI}}$). The rest of this section focuses on characterizing the background models to determine each N_i^{ROI}.

A. Methodology

The components of the background model are constructed using various combinations of calibration data, sidebands in the physics data, and simulations. For each background component, a control region (CR) is defined by an event selection in the physics data. Each CR uses different cuts, which are detailed in Secs. VII B–VII D in the context of the relevant backgrounds. Background models are tuned based on these CRs and calibration data. In addition to the low-level event selection cuts and fiducial cuts listed in Table II, a ROI is defined in $\mathrm{F}_{\mathrm{prompt}}$ vs PE space and a set of background rejection cuts are designed to remove additional backgrounds in the WIMP ROI. Target upper limits were chosen for the expectation value of each component of the background model to achieve a total expectation of $N_{\mathrm{bkg}}^{\mathrm{ROI}} < 1$. The bounds of the ROI, background rejection cuts, and fiducial cuts were tuned on the background models to satisfy the targets while maintaining the highest achievable WIMP acceptance.

The WIMP ROI is a region in $\mathrm{F}_{\mathrm{prompt}}$ vs PE space designed for sensitivity to low-energy nuclear recoils; it is defined in Sec. VIII A and spans the 95–200 PE range.

The background rejection cuts are introduced in Secs. VII B 2 and VII D 3, and they are summarized in Sec. VII E. These cuts and their effects on the WIMP acceptance, background model, and data are summarized in Table VIII.

TABLE III. Predicted number of events from each background source in the 95–200 PE of its respective CR, N^{CR} and the total number in the WIMP ROI after only low-level cuts, $N^{\mathrm{ROI,LL}}$, and after applying both fiducial and background rejection cuts, N^{ROI}. Upper limits are quoted at 90% C.L.

	Source	N^{CR}	$N^{\mathrm{ROI,LL}}$	N^{ROI}
β/γ's	ERs	2.44×10^9	0.34 ± 0.11	0.03 ± 0.01
	Cherenkov	$<3.3 \times 10^5$	<3890	<0.14
n's	Radiogenic	6 ± 4	11^{+8}_{-9}	$0.10^{+0.10}_{-0.09}$
	Cosmogenic	<0.2	<0.2	<0.11
α's	AV surface	<3600	<3000	<0.08
	AV Neck FG	28^{+13}_{-10}	28^{+13}_{-10}	$0.49^{+0.27}_{-0.26}$
	Total	N/A	<4910	$0.62^{+0.31}_{-0.28}$

Fiducialization is achieved with a set of three cuts. First, only events that reconstruct below the LAr fill level ($z < 550$ mm) and within a 630 mm radius are accepted. Two additional fiducial cuts are applied based on the fraction of total event charge in two sets of PMT rows: the bottom three rows and the top two rows, closest to the opening of the AV neck. These two cuts are discussed in Secs. VII D 2 and VII D 3, respectively.

The fiducial mass is determined using ^{39}Ar ER events in the 95–200 PE range. After applying all fiducial cuts, it is measured to be (824 ± 25) kg. The uncertainty on this value accounts for the uncertainty on the mass of the LAr target and the relative difference seen when applying these cuts to ^{39}Ar β-decay and ^{40}Ar NR simulations. Table II shows the estimated contained LAr mass as each of the three fiducial cuts is sequentially applied. The final fiducial mass is the value after all three cuts.

The number of events in the 95–200 PE range of each CR (N_i^{CR}) and the number of events in the WIMP ROI after low-level cuts ($N_i^{\mathrm{ROI,LL}}$) and after all background rejection and fiducial cuts (N_i^{ROI}) is shown in Table III. For background models using simulations, the values of N_i^{ROI} include systematic uncertainties that are derived from multiple simulations of the background source with variations in the optical model and detector response parameters. These include variations in the following: (1) the refractive index of LAr and its corresponding relationship to the scattering length and group velocity of light traveling in it, (2) the scattering length of photons in TPB, (3) the PMTs' AP probabilities, (4) the light yield of the detector, and (5) the relative PMT efficiencies. Uncertainties in the bias and resolution of the position reconstruction algorithms and the level of agreement between data and simulation for these quantities, as shown in Fig. 10, are also considered. For simulated α-decay background sources, the systematic uncertainty also includes contributions from variations in the parameters describing α-particle scintillation in LAr, the light yield of α particles in TPB (for AV surface components), and the thickness of a LAr film (for neck FG components).

The value of each N_i^{ROI} term in Eq. (8) is determined using these tuned models by applying all WIMP selection cuts to them. The remainder of this section discusses how each specific N_i^{ROI} term is determined.

B. β particles and γ-rays

The β particles and γ-rays both trigger events in the detector, either by producing scintillation light in the LAr or by creating Cherenkov light in the acrylic.

1. Scintillation in LAr

High energy electrons, produced by β-decays of radioisotopes in LAr or by γ-ray interactions in the LAr, ionize and produce scintillation characterized by low $\mathrm{F_{prompt}}$ ER events.

The dominant source of ER events is from β-decays of ^{39}Ar, as can be seen in the PE distribution shown in Fig. 4. Due to its long half-life, ^{39}Ar is present with a near-constant activity of 3.1 kBq throughout the data set. Low-energy ^{39}Ar ER events are efficiently mitigated with PSD, using the $\mathrm{F_{prompt}}$ parameter defined in Eq. (1).

The ER and NR PSD models in Eqs. (4) and (5) are used to calculate the number of ER events expected to leak past a given $\mathrm{F_{prompt}}$ value and to determine the WIMP acceptance at that value.

The CR for ER events is defined by the set of events passing low-level event selection cuts in the 95–200 PE range. No explicit $\mathrm{F_{prompt}}$ cut is applied to the CR definition, though events whose $\mathrm{F_{prompt}}$ values appear as outliers at a given PE are excluded. The expected number of events in the CR is $N_{\mathrm{ER}}^{\mathrm{CR}} = 2.44 \times 10^9$.

Figure 14 shows the fraction of ER events expected above a given $\mathrm{F_{prompt}}$ value, showing the 50% and 90% NR acceptance values. Leakage probabilities are shown for a 1 $\mathrm{keV_{ee}}$-wide window near the WIMP search threshold, corresponding to the range 95–101 PE (15.6–16.6 $\mathrm{keV_{ee}}$). In this range, a leakage fraction of $2.8^{+1.3}_{-0.6} \times 10^{-7}$ ($1.2^{+0.7}_{-0.3} \times 10^{-9}$) is predicted for cut values with 90% (50%) NR acceptance. Averaged over the full WIMP

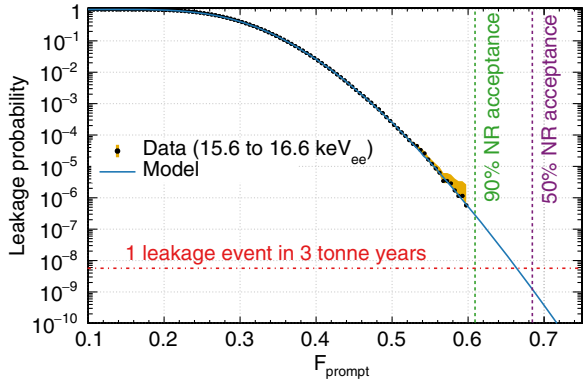

FIG. 14. Probability of an ER being detected above a given F_{prompt} value in the lowest 1 keV_{ee} bin in the WIMP-search region of interest. For comparison, vertical lines show the values above which 90% or 50% of nuclear recoils are expected to be found.

search energy range, the leakage probability is projected to be $4.1^{+2.1}_{-1.0} \times 10^{-9}$ ($3.5^{+2.2}_{-1.0} \times 10^{-11}$) with 90% (50%) NR acceptance. The low leakage probabilities at these values demonstrate the power of PSD to efficiently reject ER background events.

The uncertainty in these leakage predictions is driven by uncertainty in the F_{prompt} values corresponding to the quoted NR acceptance values. Since the leakage probability decreases rapidly with F_{prompt}, small variations in the F_{prompt} value lead to relatively large variations in the leakage probability. These uncertainties therefore have little effect on the ultimate ER background prediction.

The ER spectrum is uniformly sampled throughout the data taking period and is measured in the 95–200 PE range approximating the effects of WIMP search cuts and correcting the observed spectrum for the trigger efficiency. Using this spectrum and the leakage probability estimates, the total number of leakage events above a given F_{prompt} value is predicted as a function of PE.

The F_{prompt} vs PE ROI is shown in Fig. 20; the lower left edge of the ROI, below 160 PE, is selected for an expectation of < 0.05 ER leakage events in the data set, with uniform leakage expectation over that edge. The acceptance of the ROI for NRs is shown in Fig. 21.

After applying all fiducial and background rejection cuts, $N_{ER}^{ROI} = 0.03 \pm 0.01$ ER events are expected to reconstruct inside the ROI. The uncertainty on this estimate is dominated by systematic uncertainties in the ER model fits relating to the sample size and range of the fits.

2. Cherenkov in acrylic

Electrons, either from β-decays or the scattering of γ-rays, may produce Cherenkov events in the acrylic or PMT glass. Since Cherenkov light has a significant UV component, the UVA acrylic of the AV and LGs reduce this background. As a result, most Cherenkov light generated by ^{238}U and ^{232}Th progeny in the detector materials produce too few PEs to pass the WIMP search PE threshold. Due to the short timescales (<1 ns) over which Cherenkov light is produced, the majority of these events have high F_{prompt} values, reconstructing above the upper F_{prompt} bound of the WIMP ROI.

The detector response to Cherenkov light is characterized using a series of dedicated ^{232}U source calibration runs taken during the data collection period. In these calibration runs, the dominant production mechanism for Cherenkov events is from 2.61 MeV γ-rays emitted by ^{208}Tl at the bottom of the chain. In each calibration run, the source was deployed through one of several calibration tubes located close to the outside of the stainless steel shell. Two primary locations are used: the equator of the stainless steel shell and close to the bottom of the AV neck. Two Cherenkov populations are identified based on the ratio N_{hit}/PE, where N_{hit} is the number of PMTs registering hits in the event; this ratio provides a measure of how diffuse the light is. The two characteristic types of Cherenkov events are from those produced in the acrylic of LGs and those produced in the AV neck and pentagonal regions between LGs. The distributions of detected PEs across PMTs in these two populations are different and inform the cuts defined to remove them.

Light from Cherenkov in the LGs is highly localized; such events are mitigated by removing events with more than 40% of the total event charge in one PMT. This cut has a negligible effect on the WIMP acceptance. However, it contributes to a small live time loss in the analysis, as described in Sec. VI A.

The AV neck and pentagonal regions are less photon-sensitive than other regions of the detector; Cherenkov light produced in these regions can appear more diffuse than in the LGs. Events generated in pentagonal regions are rejected by the fiducial radius cut. Visible Cherenkov light produced in the neck region can travel through the acrylic of the neck and reach the optical fibers of the NV. Events that generate a signal in at least one NV PMT are cut. The probability that light from LAr scintillation triggers the NV after being shifted by the TPB is factored into the total WIMP acceptance as shown in Table VIII.

The WIMP ROI is used as the CR to characterize these events, after only applying cuts to remove pileup events and self-diagnostic triggers from the DAQ. Each of the two Cherenkov populations are studied in ^{232}U calibration runs. For both populations, the ratio of events generated in the WIMP ROI to those in a higher F_{prompt} sideband is measured. This sideband is defined as the region of the F_{prompt} vs PE plane above the WIMP ROI extending to $F_{prompt} = 1$, across the same 95–200 PE range. The rates of both Cherenkov populations in this sideband are measured in the physics data, and this ratio is used to estimate their leakage rates into the WIMP ROI.

The predicted number of LG Cherenkov events in the WIMP ROI after only applying the CR cuts is $< 325\,000$

(90% C.L.). For the AV neck and pentagonal Cherenkov events, it is < 3890 (90% C.L.). Combined, the total is $N_{\mathrm{Cher}}^{\mathrm{CR}} < 3.3 \times 10^5$ (90% C.L.).

To determine the respective fractions of events that survive all WIMP selection cuts, all cuts are applied to both populations in the high F_{prompt} sideband. An upper limit on the fraction of LG Cherenkov events surviving all cuts is determined to be $< 4.62 \times 10^{-7}$ (90% C.L.). For the AV neck and pentagonal Cherenkov events an upper limit of $< 6.13 \times 10^{-5}$ (90% C.L.) is calculated. The number of events in the WIMP ROI after all event selection cuts for each population is < 0.11 (90% C.L.) for LG Cherenkov events, and < 0.09 (90% C.L.) for AV neck and pentagonal Cherenkov events. These combine to produce an expectation of $N_{\mathrm{Cher}}^{\mathrm{ROI}} < 0.14$ events (90% C.L.).

C. Neutrons

Neutrons can be produced by radiogenic and cosmogenic processes. A neutron can scatter on an Ar nucleus and produce a NR event, exactly like that expected from a WIMP. However, these recoils generally reconstruct with different PE and position distributions than expected from WIMPs. These and other differences make it possible to study neutrons outside of the WIMP ROI to inform a prediction of their background rate.

1. Radiogenic neutrons

Radiogenic neutrons can be produced by the (α, n) reaction induced by α-decays in the ^{238}U, ^{235}U, and ^{232}Th decay chains, or by the spontaneous fission of ^{238}U. These isotopes are present in trace quantities in detector components. The neutron production rate was controlled by careful material selection and an extensive material assay campaign. The assay results for the materials used in DEAP-3600 are given in [10].

Based on these assays, the neutron flux and energy spectra from each detector component is determined using SOURCES-4C [41] and NeuCBOT [42]. GEANT4 simulations propagate neutrons through the detector to predict the number that will induce WIMP-like backgrounds from each source.

The polyethylene filler blocks between LGs and borosilicate glass in the AV PMTs are the dominant sources of neutron backgrounds, followed by the polystyrene filler foam between LGs, the ceramic in the PMTs, the polyvinyl chloride (PVC) PMT mounts, and the NV PMTs. The predicted contributions from these neutron sources are summarized in Table IV. All other detector components are found to have a negligible contribution to the total background rate. Uncertainties shown in this table are both statistical and systematic, including uncertainties in the assay results and the simulation's optical model and detector response as outlined in Sec. VII A. The dominant uncertainty comes from the level of ^{238}U contamination in the filler blocks.

TABLE IV. Predicted number of neutron backgrounds from simulations, using (α, n) yields calculated by either SOURCES-4C or NeuCBOT, for the dominant sources. All fission yields are calculated using SOURCES-4C. Background rates are calculated within a CR used for validating the neutron background model *in situ*, and within the WIMP ROI.

	CR prediction	
Component	(SOURCES-4C)	(NeuCBOT)
PMT glass	$2.4^{+1.2}_{-0.8}$	$4.1^{+2.0}_{-1.3}$
PMT ceramic	$0.22^{+0.06}_{-0.11}$	$0.36^{+0.09}_{-0.15}$
PMT mounts	$0.095^{+0.032}_{-0.041}$	$0.10^{+0.04}_{-0.05}$
Filler blocks	$7.1^{+8.2}_{-7.0}$	$8.1^{+9.2}_{-7.7}$
Filler foam	$0.79^{+0.43}_{-0.41}$	$0.95^{+0.50}_{-0.47}$
Neck PMTs	$0.038^{+0.022}_{-0.032}$	$0.060^{+0.036}_{-0.049}$
Total	$10.6^{+8.3}_{-7.1}$	$13.6^{+9.4}_{-7.8}$
	ROI prediction	
Component	(SOURCES-4C)	(NeuCBOT)
PMT glass	$0.009^{+0.008}_{-0.004}$	$0.016^{+0.013}_{-0.007}$
PMT ceramic	<0.02	<0.03
PMT mounts	$0.0004^{+0.0002}_{-0.0001}$	$0.0004^{+0.0003}_{-0.0001}$
Filler blocks	$0.042^{+0.102}_{-0.042}$	$0.048^{+0.115}_{-0.048}$
Filler foam	$0.0076^{+0.0107}_{-0.0063}$	$0.0088^{+0.0123}_{-0.0067}$
Neck PMTs	<0.01	<0.02
Total	$0.060^{+0.104}_{-0.045}$	$0.073^{+0.119}_{-0.048}$

To validate the neutron background prediction, a CR is defined, extending to 5000 PE with a loose cut requiring $0.6 < F_{\mathrm{prompt}} < 0.8$, a radial cut of < 800 mm, and low-level event selection cuts applied. NR-like events within this CR are identified, and high-energy ER events above 1.4 MeV are counted within a 1 ms coincidence window following the NR.

Due to the abundance of ^{1}H in acrylic and the efficient kinematic coupling between ^{1}H and neutrons, most neutrons that scatter in the LAr are expected to thermalize within a few centimeters after leaving the LAr and entering the AV, while a smaller fraction may thermalize in the LAr. Those that thermalize in the acrylic will predominantly capture on ^{1}H and produce a 2.2 MeV γ-ray, while those that are captured on ^{40}Ar in the LAr will produce multiple γ-rays summing in energy to 6.1 MeV. The thermal neutron capture time in acrylic is 250 μs and in LAr is 325 μs, meaning that over 95% of all neutrons that scatter in the LAr will capture within this 1 ms coincidence window following the NR.

GEANT4 simulations indicate that the probability of detecting a neutron capture event given that the neutron produced a NR in the CR is approximately independent of

the origin of the neutron. By counting the number of NRs followed by a capture γ-ray signal, the number of neutron-induced events within the CR can therefore be determined.

To account for accidental coincidences, where a NR not caused by a neutron is followed by a random γ-ray, a "random coincidence" sideband window is considered. This window extends for 19 ms, starting after the end of the coincidence window. The number of NRs followed by a signal within the random coincidence window is counted and scaled down by a factor of 19 to provide an estimate of the expected number of accidental coincidences during this search.

To determine the tagging efficiency of this method, this coincidence search is applied to AmBe neutron calibration source data, where it is found to tag $(22.5 \pm 0.5)\%$ of neutron-induced NRs. This efficiency is consistent with simulations, which indicate that the primary source of inefficiency is from neutrons that capture on ^{1}H in the acrylic and produce a γ-ray that loses more than 800 keV in volumes other than the LAr.

Applying this search to the data reveals 7 coincidence events in the CR—none of which falls in the ROI or appears with coincident signals in the MV—with an expectation of 1.8 ± 0.3 random coincidences. Correcting for the tagging efficiency, this gives a total of 23^{+17}_{-14} neutrons in the CR, consistent with the prediction in Table IV. This corresponds to $N^{\mathrm{CR}}_{n,\mathrm{rdg}} = 6 \pm 4$ events in the 95–200 PE range of the WIMP ROI after applying the CR cuts.

Simulations of neutrons coming from the PMTs or from the outer surface of the AV give consistent ratios of events in the CR to those in the WIMP ROI, after all event selection cuts. Scaled by this ratio, the observed number of events in the CR predict $N^{\mathrm{ROI}}_{n,\mathrm{rdg}} = 0.10^{+0.10}_{-0.09}$ neutron-induced backgrounds in the WIMP ROI after all WIMP selection cuts.

2. Cosmogenic neutrons

Cosmogenic neutrons are produced by high-energy atmospheric muon interactions with the detector and its environment. The 6 km water-equivalent overburden of SNOLAB provides a significant reduction to the muon flux experienced by DEAP-3600. The MV allows events induced by muons reaching the detector to be vetoed by the Cherenkov signal they produce in the water of the MV water tank.

Muons are tagged either directly when they pass through the MV, or indirectly when they produce an electromagnetic shower in the laboratory whose charged products enter the MV. These events are identified in MV triggers in which significantly more light is seen in the detector than can be explained by noise or by normally present γ-rays. By counting the number of muons passing through the MV, a flux of $(3\text{–}4) \times 10^{-10}$ muons/cm^2/s is measured, consistent with the flux of $(3.31 \pm 0.10) \times 10^{-10}$ muons/cm^2/s reported by SNO [43].

Normalizing to the flux reported in [43] and simulating muons with the energy spectra described by [44] results in a prediction of $N^{\mathrm{CR}}_{n,\mathrm{csg}} < 0.2$ in the cosmogenic neutron CR, defined as the WIMP search ROI with only low-level cuts applied. After applying all fiducial and background rejection cuts, this prediction becomes $N^{\mathrm{ROI}}_{n,\mathrm{csg}} < 0.11$ prior to any cuts with the MV PMTs. These simulations model neutrons below 20 MeV using the "high-precision" (HP) GEANT4 physics models, and the default GEANT4.9.6 hadronic physics models for higher energy neutrons.

The MV is used to further reduce the rate of these background events. A cut has been designed to tag muons passing through the MV based on the number of PMTs hit and the number of PEs detected, in order to identify events in which a significant signal is seen above the baseline background of noise in the MV. Events in the AV are vetoed if they fall within a $[-0.1, 1]$ s window around the tagged event. This cut reduces the live time by 0.16%, mostly due to accidental veto triggers not caused by muons.

D. α particles

Signals from α-decays from short- and long-lived ^{222}Rn progeny as well as short-lived ^{220}Rn progeny are observed at several locations inside the detector. These include the LAr target, the LAr/TPB and TPB/AV surfaces, and the surfaces of the acrylic flow guides in the AV neck. A summary of the measured activities or event rates for these α-decays is provided in Table V.

TABLE V. Activity (Bq) or event rate (Hz) of different short- and long-lived α-decays in the detector. Values are quoted for per kg of LAr and per m^2 of the TPB or AV surface. Upper limits are quoted as 90% C.L. The value quoted for ^{212}Bi accounts for both α-decay (36%) and β-decay (64%) modes. Rates on the FGs are quoted for the inner surface (IS) and outer surface (OS).

	Component	Activity/Rate
Short-lived α-decays	^{222}Rn LAr	(0.153 ± 0.005) μBq/kg
	^{218}Po LAr	(0.159 ± 0.005) μBq/kg
	^{214}Po LAr	(0.153 ± 0.005) μBq/kg
	^{214}Po TPB surface	<5.0 μBq/m^2
	^{220}Rn LAr	(4.3 ± 1.0) nBq/kg
	^{216}Po LAr	(4.5 ± 0.4) nBq/kg
	^{212}Bi LAr	<5.6 nBq/kg
	^{212}Po LAr	(3.4 ± 1.1) nBq/kg
Long-lived α-decays	^{210}Po TPB & AV surface	(0.26 ± 0.02) mBq/m^2
	^{210}Po AV (bulk)	(2.82 ± 0.05) mBq
	^{210}Po inner FG, IS	(14.1 ± 1.3) μHz
	^{210}Po inner FG, OS	(16.8 ± 1.4) μHz
	^{210}Po outer FG, IS	(22.7 ± 1.6) μHz

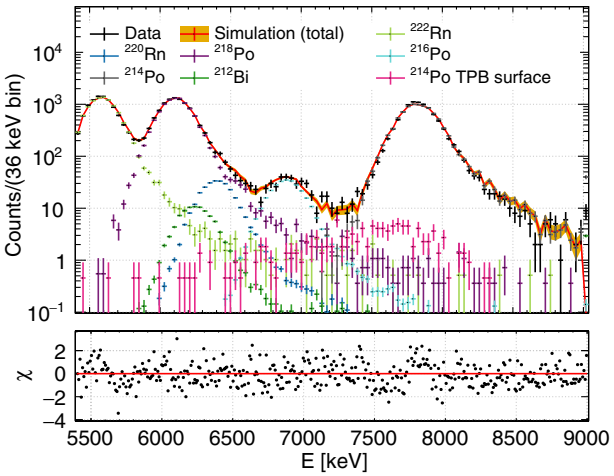

FIG. 15. Distribution of mapped α-particle energies from F_{prompt} and PE for short-lived α-decays in LAr. The event selection shown has no cut on position reconstruction and so includes events from ^{214}Po α-decays at the TPB surface (purple).

1. Short-lived α-decays

The primary sources of short-lived α-decays are from ^{238}U progeny: ^{222}Rn, ^{218}Po and ^{214}Po (and its daughters) with emitted α-particle energies of 5.5 MeV, 6.0 MeV and 7.7 MeV, respectively. A subdominant event rate is observed from α-decays of ^{232}Th progeny: ^{220}Rn, ^{216}Po, ^{212}Bi and ^{212}Po (and its daughters) with respective emitted α-particle energies of 6.3, 6.8, 6.1 and 8.8 MeV.

These α-decays occur in the LAr, appearing as high-energy events in the 23 000–50 000 PE range at high F_{prompt}. To determine their activities, low-level cuts are applied, and a fit to the data is performed by first applying an analytical correction which maps F_{prompt} and PE to α-particle energy in units of keV. This mapping corrects for the effect of digitizer and PMT saturation on PE and F_{prompt}. Simulations of different α-decays are used, to which an equivalent correction is applied in order to produce energy spectra.

A binned log-likelihood fit of these simulated spectra to the spectrum observed in data allows for individual activities of each component to be determined. These spectra and the spectrum observed in data are shown in Fig. 15. The fit includes the following α-decay components in LAr (in order of increasing α-decay energy): ^{222}Rn, ^{218}Po, ^{212}Bi, ^{220}Rn, ^{216}Po and ^{214}Po. In addition, a component of ^{214}Po simulated at the LAr/TPB interface is included to allow for a plate-out fraction of ^{214}Po to be resolved. The plate-out of nuclei on surfaces such as the TPB is possible over the timescale in which the parent ^{222}Rn nucleus decays ($t_{1/2} = 3.8d$).

Events caused by the α-decay of ^{212}Po (8.8 MeV) are observed in the data set; however, this component is omitted from the fit. Due to its very short half-life ($t_{1/2} = 299$ ns), ^{212}Po reliably appears as pileup with the β-decay of its parent ^{212}Bi within the same time window of a single triggered event. This effect smears PE and F_{prompt} over a broad range of values, migrating the majority of the events out of the fit region.

The activity of ^{212}Po is calculated independently using a simulation of ^{212}Bi-decays to estimate the selection efficiency for observing the ^{212}Po α-decay in the fit region. The estimated activity of ^{212}Po using this method is (3.4 ± 1.1) nBq/kg and is consistent with the activity of ^{212}Bi (<5.6 nBq/kg) from the fit. Assuming the ^{212}Bi $\rightarrow$ ^{212}Po β-decay mode branching fraction of 64% and secular equilibrium, it is also in agreement with the measured rates of ^{220}Rn and ^{216}Po.

These high-energy events in the LAr target do not contribute to backgrounds in the WIMP ROI.

2. Long-lived α-decays: AV surface

Nuclei that α-decay on the inner surfaces of the detector or on visible interfaces between two components (such as the LAr/TPB and TPB/AV interfaces) or inside of these components may produce signals from α particles with degraded energies. As a result, these events may produce fewer PEs and have a larger impact on the WIMP search than those from nuclei that are distributed throughout the LAr.

The primary source of α-decays from surfaces is ^{210}Po ($t_{1/2} = 138$ d) from the inner surface of the AV. Note that ^{210}Po appears later in the ^{222}Rn decay chain than ^{210}Pb, which has a half-life of 22.3 yr. As such, it may appear on detector surfaces out of equilibrium with other isotopes in this decay chain.

Events resulting from these decays peak in the 18 000–22 000 PE range and extend to lower PE as shown in Fig. 16. This distribution is obtained by applying low-level cuts and selecting events with $F_{prompt} > 0.55$ that reconstruct with a z-position below the LAr fill level. It is fit with a model of the ^{210}Po surface activity, which is built with simulated spectra, with additional smearing introduced to match the data. The model features three components of ^{210}Po activity: (1) a surface component at the LAr/TPB interface and throughout the 3 μm TPB layer, (2) a second surface component at the TPB/AV interface, and (3) a bulk component of ^{210}Po decays occurring up to 50 μm beneath the inner surface of the AV. Simulations predict no triggers from ^{210}Po α-decays beyond this depth. A component of the ^{222}Rn α-decays spectrum in LAr that is close to the ^{210}Po spectra in energy is also included in the fit. This component helps constrain the ^{210}Po contributions in the TPB layer and at the LAr/TPB interface.

Not all α-decays on detector inner surfaces result in a trigger. The combined surface activity of ^{210}Po is measured to be (0.26 ± 0.02) mBq/m^2. From the bulk component it is measured to be (2.82 ± 0.05) mBq. This yields event rates of (1.31 ± 0.11) mHz from all surface decays and (0.51 ± 0.02) mHz from the bulk component.

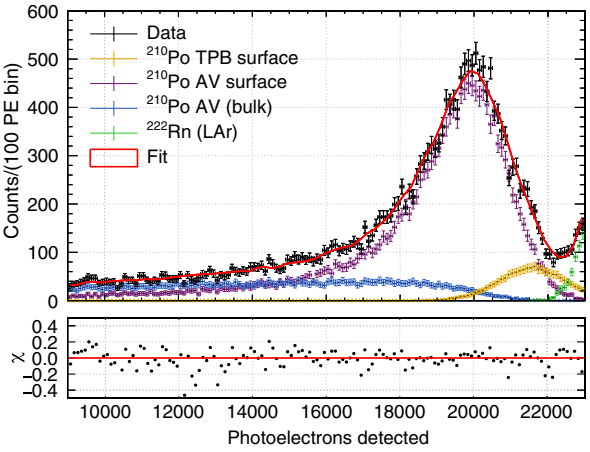

FIG. 16. PE distribution from data of ^{210}Po α-decays candidates (black) alongside different simulated ^{210}Po samples located on the AV surface at the TPB/AV interface (purple), at the LAr/TPB interface and within the TPB layer (yellow), and from beneath the inner surface of the AV (blue). Shown also is the neighboring PE distribution from ^{222}Rn α-decays in LAr (green). Overlaid is the combined fit (red) of each of these spectra to the observed PE spectrum from data. The event selections shown reconstruct with a z-position below the LAr fill level. No cut on the reconstructed radius is applied.

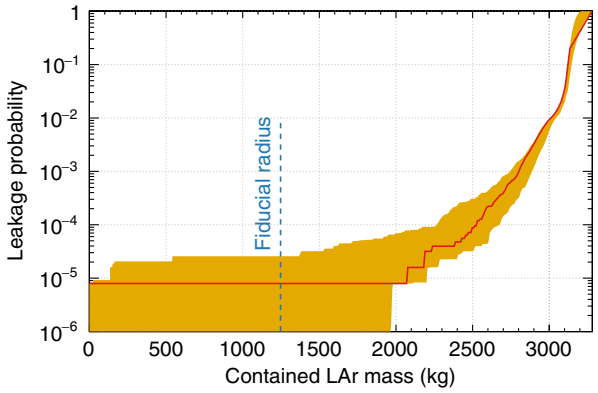

FIG. 17. Leakage probability for simulated α-decays in the WIMP PE range vs the contained LAr mass as determined by events within a given reconstructed radius. The contained LAr mass corresponding to the fiducial cut at 630 mm is shown. The systematic uncertainty on the probability is shown also (yellow band).

The CR for ^{210}Po α-decays is based on using the fitted values of the activity and the simulations to predict the event rate at low energies in the 95–200 PE range. In this CR, $N^{\mathrm{CR}}_{\alpha,\mathrm{AV}} < 3600$ (90% C.L.) ^{210}Po α-decay events are predicted before applying any cuts. As a cross-check, a search for these events inside the WIMP ROI is performed on the entire data set, and 1461 candidate events are counted. None of these events survives the fiducial cuts.

A measurement of the leakage probability, defined as the fraction of events that reconstruct within a given volume, is calculated using a simulation of α-decays at the LAr/TPB interface. As shown in Fig. 17, in the 95–200 PE range, the leakage fraction is $0.8^{+1.8}_{-0.8} \times 10^{-5}$ for the LAr mass contained within the fiducial radius. In this analysis, $N^{\mathrm{ROI}}_{\alpha,\mathrm{AV}} < 0.08$ (90% C.L.) events from AV surface decays are predicted after all event selection cuts in the WIMP ROI.

In the 10 000–20 000 PE range of Fig. 16, two observations are made: (1) 5% of the events reconstruct with a radius < 630 mm, and (2) an excess of events is observed reconstructing towards the bottom of the detector. Neither of these observations is predicted by the model in this PE range. The excess appears for events reconstructing both inside and outside the fiducial radius. A similar excess is observed at lower energies, in a 200–1000 PE sideband of the WIMP ROI. To mitigate potential events of this type from the dark matter search, an additional cut is applied to remove events where 10% or more of the total event charge is contained in the bottom three rows of PMTs. The cut value is determined from events in the 200–1000 PE sideband, where 99% of the excess events are removed by the cut.

This cut fiducializes against events originating from the bottom of the AV and hence features in the fiducial cut selection in Table II. It is not solely responsible for removing any events from the WIMP ROI, and it does not remove all events in the sideband. These excess events are being investigated, and it is not yet known if the excess at high PE is related to the excess in the low PE sideband. One explanation being considered, among others, is a low level of particulate contamination in the LAr.

3. Long-lived α-decays: AV neck

The largest contribution to the background rate after applying fiducial cuts is from ^{210}Po α-decays on the surfaces of the acrylic FGs in the AV neck. The neck contains two separate FGs, referred to as the inner and outer FGs (IFG and OFG). There are three distinct surfaces on these components: the IFG's inner and outer surfaces (IFG-IS and IFG-OS) and the OFG's inner surface (OFG-IS). These surfaces are illustrated in Fig. 18. The outer surface of the outer FG has no direct line of sight to the AV; it is coupled to the wall of the AV neck. The FGs are located in the GAr buffer region above the fill level of the LAr target. Scintillation light is observed from events in the neck, which are simulated with a thin LAr film coating the FGs. Simulations show that α particles emitted by ^{210}Po α-decays generate up to 5000 PE in the AV PMTs when they scintillate in this film. The FGs are not coated in TPB, and the acrylic absorbs most of the UV scintillation photons incident on their surfaces. This results in shadowed event topologies in which only a small fraction of the emitted photons reach the AV PMTs. The number of PEs produced by an α-decay on the FG surfaces is therefore determined by the location of the decay.

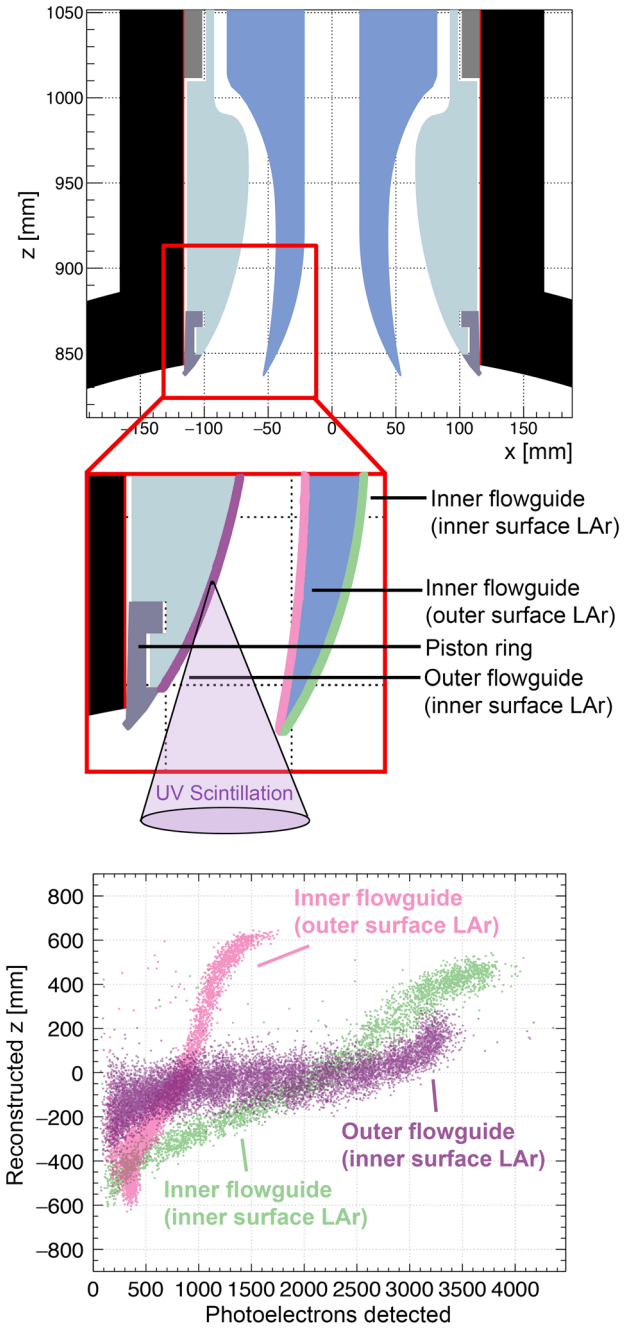

FIG. 18. Top and middle panels: Cross-sectional illustration of the FG components in the AV neck. Shown are the three FG surfaces and the piston ring (not coated in LAr for purposes of illustration). Bottom panel: Simulated relationship in reconstructed z vs PE for α-decays on the IFG-IS (green), IFG-OS (pink), and OFG-IS (purple).

The mean F_{prompt} value observed for α-decays in the neck is constant up to 5000 PE, consistent with the model prediction for 5.3 MeV α-particle scintillation in LAr. This suggests that these events are predominantly from ^{210}Po α-decays. As a cross-check, a ^{214}Bi-^{214}Po coincidence search on these events was performed, looking for ^{214}Bi γ-rays in coincidence with α-decays in the neck. This search provided no evidence that a significant fraction of these events are caused by α-decays of other ^{238}U progeny.

The shadowing of UV scintillation in the AV neck causes distinct charge distributions across the PMTs for each FG surface. These distributions produce trends in events' reconstructed z-positions that vary with PE in distinct ways, as illustrated in Fig. 18.

These distributions are used to identify different sample regions within the reconstructed z vs PE plane, in which a template fit is performed in the 300–4600 PE range. After low-level cuts, events in this energy range with $F_{prompt} > 0.55$ are selected, and two additional cuts are applied: a loose fiducial cut requiring that the reconstructed z-position be < 600 mm and a cut removing events in which more than 3.5% of the total event charge is contained within single PMT. The latter cut reduces the number of AV surface events from the event selection. This fit makes use of simulated distributions for ^{210}Po α-decays on each of the three FG surfaces, shown in Fig. 19. A flat background obtained from a 5000–8000 PE sideband is also included

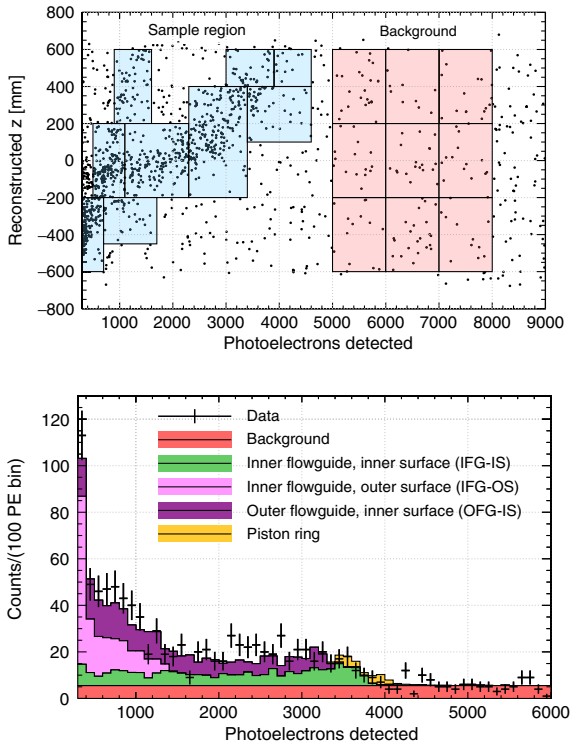

FIG. 19. Top: Distribution of reconstructed z vs PE for events at high F_{prompt} in data, using the PE-based algorithm. Shown are trends from α-decays in the neck between 300–5000 PE and a background sideband at higher PE values. The blue boxes denote the sample regions used by the template fit to compare with spectra from simulations. The red boxes are used to sample a background component. Bottom: 1D-projection of the observed PE spectra (black points) and expected distributions from the background model components, normalized to the best-fit rates.

TABLE VI. Summary of the uncertainty on the overall number of events remaining in the WIMP ROI after applying all background rejection and fiducial cuts. Uncertainties are quoted for each FG surface component.

	Uncertainty [%]		
Systematic	IFG-IS	IFG-OS	OFG-IS
Refractive index	$^{+7}_{-42}$	$^{+25}_{-10}$	$^{+13}_{-10}$
TPB scattering length	$^{+86}_{-29}$	$^{+28}_{-21}$	$^{+19}_{-0}$
Afterpulsing prob.	$^{+26}_{-36}$	$^{+0}_{-32}$	$^{+4}_{-24}$
Light yield	$^{+54}_{-0}$	$^{+0}_{-6}$	$^{+13}_{-4}$
Rel. PMT eff.	$^{+8}_{-0}$	$^{+0}_{-13}$	$^{+0}_{-29}$
α particle F_{prompt}	$^{+83}_{-50}$	$^{+58}_{-42}$	$^{+80}_{-47}$
Reconstructed radius	$^{+0}_{-75}$	$^{+0}_{-31}$	$^{+0}_{-26}$
LAr film thickness	$^{+104}_{-0}$	$^{+0}_{-49}$	$^{+0}_{-66}$
Combined	$^{+170}_{-110}$	$^{+69}_{-83}$	$^{+85}_{-80}$

in this fit, along with a simulated PE distribution from ^{210}Po α-decays in a LAr film on the AV piston ring. The piston ring contributes a small amount to the event rate in the 3000–4000 PE range. The α-decays on the piston ring were independently studied and found to have a negligible contribution to the background rate in the WIMP ROI; scintillation events on this surface are shadowed too little to populate the WIMP PE range. The fit result predicts the following event rates for each FG component before applying any cuts: (14.1 ± 1.3) μHz (IFG-IS), (16.8 ± 1.4) μHz (IFG-OS) and (22.7 ± 1.6) μHz (OFG-IS).

The model of the LAr film discussed here assumes that the FGs and piston ring are completely coated with a uniform 50 μm-thick layer of LAr. This is thick enough for the α particle to stop in the LAr, resulting in an F_{prompt} distribution consistent with the one observed in the data. Variations on the model with thinner films allow for a contribution of GAr scintillation; these scenarios are factored into the systematic uncertainty. The fraction of the FG surfaces coated in LAr is not yet known, so the event rates cannot be converted into activities. This does not impact the prediction of the event rate in the WIMP ROI based on the result of the fit.

The CR for α-decays in the AV neck consists of the WIMP ROI and low-level event selection cuts. In the CR, the model predicts 12^{+9}_{-7}, 8^{+6}_{-5}, and 8^{+7}_{-5} events from the IFG-IS, IFG-OS, and OFG-IS, respectively. These values give a total expectation of $N^{CR}_{\alpha,neck} = 28^{+13}_{-10}$. These uncertainties are dominated by systematic uncertainties in the background model; their effects on the background expectation of α-decays on the FGs after all background rejection and fiducial cuts are summarized in Table VI.

The dominant systematic uncertainties are related to the model of α-particle scintillation parameters and the thickness of the LAr film, variations of which can make reconstructed events migrate in or out of the ROI. In addition, changes to the TPB scattering length have a significant impact on the fraction of events that survive fiducial cuts. UV photons incident on the TPB layer of the AV can be backscattered away from the PMTs, producing an inward bias to the reconstructed radius position. It is particularly relevant to sources of collimated UV light such as those generated by α-decays in the neck.

TABLE VII. Predicted rejection efficiency of each cut to remove events generated by α-decays from each of the three FG surfaces. The efficiency is calculated for events with a reconstructed radius < 630 mm in the range of 95–200 PE. These efficiencies are determined from simulations. The last row provides an estimate of the combined rejection efficiency after applying all four cuts.

	Neck α-decay rejection [%]		
Cut name	IFG-IS	IFG-OS	OFG-IS
Upper F_{prompt} cut	73	59	72
Early pulses in GAr PMTs	80	85	81
Charge fraction in top 2 rows of PMTs	57	46	36
Position reconstruction consistency	90	93	82
Combined	99	99	98

The distinctive F_{prompt} and z vs PE distributions produced by α-decays in the AV neck distinguish them from NR events originating in the LAr target. Cuts have been developed to use this information and were optimized such that the WIMP acceptance is maximized while maintaining a background expectation below the target of < 0.5 events from all FG components. A summary of the rejection efficiency for each cut removing these events is shown in Table VII. The reported rejection efficiencies are for events reconstructing inside the 630 mm fiducial radius and in the 95–200 PE range. These cuts are described in more detail below.

Upper F_{prompt} *cut*.—The α-decays with initial energies of 5.3 MeV produce systematically higher F_{prompt} values than are expected from NRs in the WIMP ROI, as shown in Fig. 20. The upper F_{prompt} bound of the ROI therefore removes a significant fraction of α-decays in the neck, at the cost of 30% acceptance loss to signal events.

Early pulses in GAr PMTs.—The origin of UV scintillation light from these events is above the fill level of the LAr. PMTs whose LGs subtend the GAr region just above the LAr fill level will register PEs from UV photons reflecting from the GAr/LAr interface before PMTs located further down do so. This effect is aided by the fact that the group velocity of UV light in GAr is almost 3 times that in LAr. The location of PMTs that register the first pulses in the PE integration window can be used to remove α-decays in the AV neck. The rejection power of this cut improves as the number of detected PEs increases. At higher PE more UV photons enter the AV, increasing the probability of UV photons reflecting from the GAr/LAr

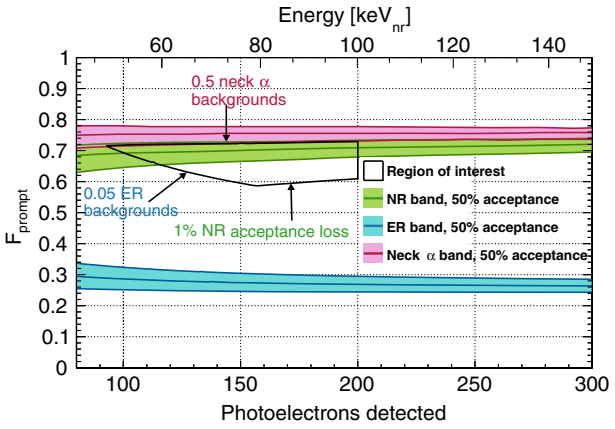

FIG. 20. Illustration of the WIMP ROI (black) along with the ER (blue), NR (green), and neck α-decay (pink) bands that define the boundaries. Each band is drawn about the median of each class of events, with 25% of such signals above and 25% below included in the shaded regions.

interface and reaching a PMT in the GAr region first. Events are rejected if any of the first 3 pulses observed in the PE integration window are registered in PMTs that subtend the GAr region. Based on simulations, a value of 3 was found to be the minimum number of pulses required to reach the neck α-decay background target of <0.5 events when combined with all other cuts, without requiring other cuts to induce an even larger acceptance loss. This cut is the largest source of loss in signal acceptance within the fiducial volume. However, it is a simple model-independent method of fiducializing against backgrounds with topologies strongly affected by the LAr/GAr interface.

Charge fraction in top 2 rows of PMTs.—Due to the reflection of UV photons at the GAr/LAr interface, a larger fraction of PEs are seen by PMTs above the fill level for α-decays in the neck than for WIMP-like recoils in the LAr target. Events that have $\geq 4\%$ of the total observed charge seen in the top 2 rows of PMTs (10 PMTs in total) are removed. This cut is a charge-based equivalent of the early pulses in the GAr PMT cut, removing events close to the LAr/GAr interface. These two cuts are correlated but are found to both be necessary in order to achieve the desired background level.

Position reconstruction consistency.—Scintillation events originating in the neck produce distinct hit patterns in each channel compared to events originating in the LAr target. Since both position reconstruction algorithms are trained on scintillation events in the LAr target, they generally reconstruct such events at similar positions, as demonstrated in Fig. 12. However, the algorithms give systematically different results for events originating in the neck. The PE-based algorithm systematically reconstructs these events lower in the detector than is predicted by the time residual-based algorithm. To remove events coming from the neck, a consistency cut is used, removing events where the time residual-based algorithm reconstructs an event significantly higher in the detector than the PE-based algorithm did or where both algorithms reconstruct the event far from each other. Events are rejected if the time residual-based algorithm returns a z coordinate higher than the PE-based algorithm, with a difference that is more than what would be expected for 90% of LAr scintillation events. If an event passes this cut, a further criterion is required: the distance between both estimated positions must be within the expected range for 85% of LAr scintillation events. The cut value for both consistency criteria is a function of prompt PE.

After applying all fiducial and background rejection cuts, $0.07^{+0.13}_{-0.07}$, $0.17^{+0.12}_{-0.14}$, and $0.25^{+0.21}_{-0.20}$ events from the IFG-IS, IFG-OS and OFG-IS components are expected in the WIMP ROI, respectively. This combines to an overall expectation of $N^{\mathrm{ROI}}_{\alpha,\mathrm{neck}} = 0.49^{+0.27}_{-0.26}$ events in the data set.

E. Summary of backgrounds

After applying all fiducial and background rejection cuts to the data, no events remain in the WIMP ROI. Table VIII summarizes the background rejection cuts and their cumulative effect on the WIMP acceptance after applying all fiducial cuts. The acceptance is determined using ^{39}Ar ER signals in the 95–200 PE range, as was done for the calculation of the fiducial mass in Sec. VII A. Similarly, the systematic uncertainty is derived from the level of agreement of these cuts to select simulated ^{39}Ar ER and ^{40}Ar NR events. Table VIII also shows the total predicted number of ROI events, $N^{\mathrm{ROI}}_{\mathrm{bkg}}$, compared to the number observed in the data set, $N^{\mathrm{ROI}}_{\mathrm{obs}}$.

TABLE VIII. Cumulative impact of background rejection cuts on the WIMP acceptance, the predicted number of background events, $N^{\mathrm{ROI}}_{\mathrm{bkg}}$, and the total number of observed background events, $N^{\mathrm{ROI}}_{\mathrm{obs}}$, after applying fiducial cuts to events inside WIMP ROI. Cuts are grouped by the background they predominantly remove. The value of the acceptance is averaged over the 95–200 PE range.

	Background rejection cut	WIMP accept. [%]	$N^{\mathrm{ROI}}_{\mathrm{bkg}}$	$N^{\mathrm{ROI}}_{\mathrm{obs}}$
Cherenkov	Neck veto	$92.0^{+1.0}_{-0.1}$	$9.2^{+4.4}_{-3.5}$	29
α-decays in neck	Early pulses in GAr PMTs	$45.4^{+1.5}_{-0.1}$	$2.3^{+1.1}_{-0.9}$	2
	Position fitter consistency	$35.4^{+2.5}_{-0.1}$	$0.62^{+0.31}_{-0.28}$	0
	Total	$35.4^{+2.5}_{-0.1}$	$0.62^{+0.31}_{-0.28}$	0

VIII. WIMP SEARCH ANALYSIS

Once all WIMP event selection cuts have been applied to the data, the number of events remaining in the WIMP ROI is used to place an upper limit at the 90% confidence level on the spin-independent WIMP-nucleon cross section.

A. ROI definition

The ROI used for the WIMP search is driven by the signal and background model. Figure 20 illustrates how the ROI is defined in the F_{prompt} vs PE plane; 50% acceptance bands are shown for events generated by ERs, NRs, and AV neck ^{210}Po α-decays. The ER and NR bands shown here are from the detector response model described in Sec. IV B; the neck α-decay band was taken from simulations of ^{210}Po surface decays on surfaces of the AV neck FGs. Since these α-decays are at energies of 5.3 MeV, their F_{prompt} values are correspondingly high. As such, these events have higher F_{prompt} values than expected from NRs originating in the LAr target, and they are discriminated against with PSD.

The lower F_{prompt} bound of the ROI is defined using two curves. In the 95–160 PE range it is defined to have a constant expected number of leakage events in each PE bin such that the total background rate of ER leakage events after all cuts are applied is < 0.05. The curve spanning the 160–200 PE range is defined such that there is a constant 1% NR acceptance loss.

The upper F_{prompt} bound of the ROI is defined to have constant NR acceptance loss, with 30% of NRs in each PE bin expected to fall above the ROI. As previously described this acceptance loss was chosen because it contributes towards achieving an expectation of < 0.5 events from α-decays in the AV neck.

The upper PE bound of 200 PE is chosen to be consistent with the energy of the upper bound used in [6], given the different light yields and energy estimators used for both analyses. Above this energy, the expected rate of α-particle- and neutron-related background events becomes larger, while a negligible fraction of WIMP events are expected.

B. WIMP acceptance

The WIMP acceptance as a function of PE is shown in Fig. 21. "Fiducial cuts" shows the probability of a WIMP-like event passing fiducial cuts. "Background rejection cuts" refers to the probability of an event passing the cuts listed in Table VIII given that it passed the low-level event selection and fiducial cuts listed in Table II. "F_{prompt} cut" refers to the probability of a NR appearing in the ROI. Figure 21 also shows the F_{prompt} cut acceptance for a ROI defined with 1% WIMP acceptance loss from the upper F_{prompt} bound, instead of 30% acceptance loss as in this analysis. This corresponds to the energy threshold that would be achievable if α-decays in the AV neck did not require a tighter cut, but an expectation of <0.05 ER leakage events were maintained. This curve demonstrates the power of PSD for discriminating against ER backgrounds while maintaining a low-energy threshold.

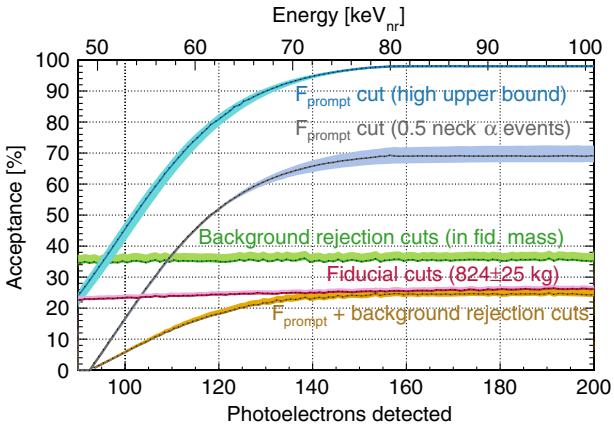

FIG. 21. WIMP acceptance as a function of PE, broken down by cut type.

C. Results

After applying all WIMP search cuts described in Tables II and VIII, the events shown in Fig. 22 remain. There are no events remaining in the region of interest. There is one event close to the ROI border, with $F_{prompt} < 0.75$ and approximately 125 PE that is above the upper F_{prompt} bound of the ROI. There are also 5 events in the 200–300 PE range with $0.55 < F_{prompt} < 1.0$. The background model discussed here is used to determine the probability that either of these two event populations is likely.

In the 95–200 PE range, the background model predicts $0.46^{+0.13}_{-0.18}$ events with F_{prompt} values between the top boundary of the ROI and $F_{prompt} < 0.75$. The probability of observing one or more events in this region is 36%, so the observed event is consistent with the model. Between 200–300 PE, a total of $1.25^{+0.26}_{-0.42}$ background events are predicted with $0.55 < F_{prompt} < 1.0$. In this region, the number of predicted events from α-decays in the AV neck

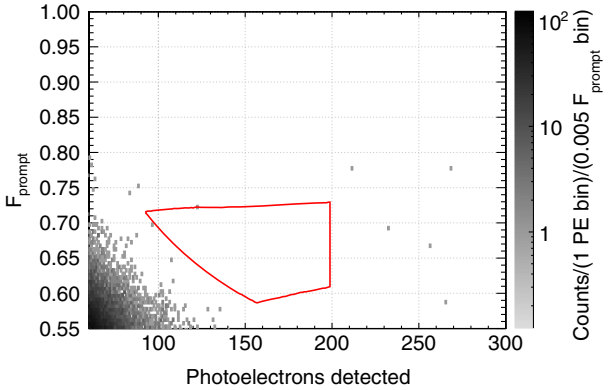

FIG. 22. Observed F_{prompt} vs PE distribution after all cuts. The region of interest is shown in red.

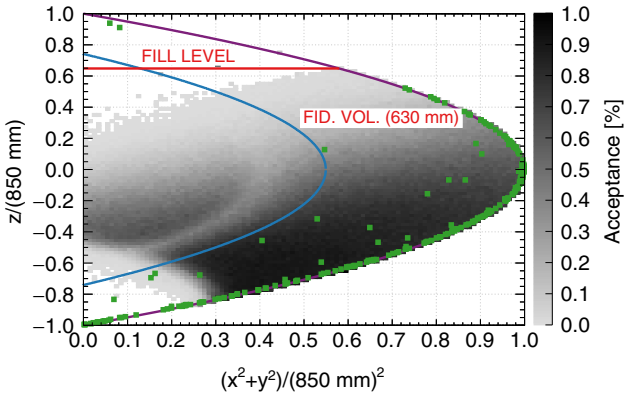

FIG. 23. Observed spatial distribution for all events surviving all cuts other than the cut on the reconstructed radius. The color scale in the background shows the acceptance for ^{39}Ar events measured as a function of position after all but the radial cut; green points represent events in the ROI after all background rejection cuts. The fill level and radial fiducial cuts are drawn as well.

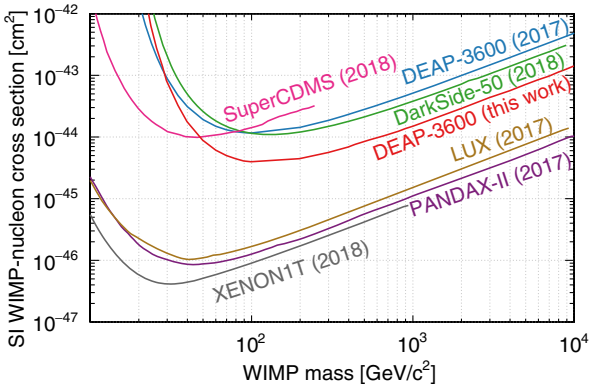

FIG. 24. The 90% confidence upper limit on the spin-independent WIMP-nucleon cross sections based on the analysis presented in this paper (blue), compared to other published limits, including our previous limit [6], SuperCDMS [46], DarkSide-50 [7], LUX [47], PANDAX-II [48], and XENON1T [5].

depends most strongly on the uncertainty in modeling the light yield for events originating in the neck. In order for the background model to be consistent with the events observed in this region, the optical properties of the neck or the position resolution must change and, in the case of the latter, by several times its uncertainty. Systematic uncertainties on optical properties of the neck relevant to events in this energy range are still being evaluated. Varying the systematic uncertainties at the required levels does not significantly affect the WIMP exclusion curve presented here. The observed excess over the nominal model extends above 300 PE. Future analyses will explore adding new background sources to the model and further constrain the relevant response functions.

Figure 23 shows the spatial distribution of events within the WIMP ROI after all event selection cuts have been applied other than the fiducial radial cut. The fill level and the fiducial radius are both shown, and the acceptance as a function of position is illustrated in the background. The fiducializing effects of the cut on the fraction of observed charge in the 2 rows of PMTs and bottom 3 rows of PMTs, as summarized in Table II, can be seen in this figure.

Figure 24 shows the 90% C.L. upper limit on the spin-independent WIMP-nucleon cross section as a function of WIMP mass. These upper limits are calculated accounting for the systematic uncertainties in the detector response function, following the prescription outlined by Highland and Cousins [45]. Uncertainties considered include those for the energy scale parameters in Table I, the PSD model fit parameters in Eq. (5), the WIMP acceptance as shown in Fig. 21, the NR quenching factors and mean F_{prompt} values, as derived from [31], and a 2.9% uncertainty on the total exposure.

This analysis excludes spin-independent WIMP-nucleon cross sections above 3.9×10^{-45} cm^2 (1.5×10^{-44} cm^2) for WIMPs with a mass of 100 GeV/c^2 (1 TeV/c^2), assuming the standard halo dark matter model described in [49], with a Maxwell-Boltzmann velocity distribution below an escape velocity of 544 km/s and $v_0 = 220$ km/s, and a local density of 0.3 GeV/cm^3.

IX. CONCLUSIONS

This work improves upon the result reported in [6], setting the most sensitive limit for the spin-independent WIMP-nucleon cross section achieved using a LAr target for WIMPs with mass greater than 30 GeV. These results are complementary to results reported by liquid xenon-based experiments, allowing for further constraints on the nature of the WIMP-nucleon coupling [50,51].

The use of LAr here demonstrates the power of PSD as a tool to achieve low backgrounds in WIMP searches, emphasizing the future prospect of much larger LAr-based detectors designed to achieve sensitivity to WIMP interaction cross sections at the level of the neutrino floor.

Additionally, a detailed description of backgrounds in the detector has been presented alongside the analysis methods and simulation models which characterize them. Using these models, a total background expectation of <1 event has been achieved; this model is consistent with observations in data in the ROI. Multivariate techniques are currently being explored to utilize these models to maximize the sensitivity to dark matter signals. Since the end of the data collection period presented here (October 31, 2017), DEAP-3600 has continued to collect data. Updated results including a blind analysis of additional data are planned for the near future.

ACKNOWLEDGMENTS

This work is supported by the Natural Sciences and Engineering Research Council of Canada, the Canadian Foundation for Innovation (CFI), the Ontario Ministry of

Research and Innovation (MRI), and Alberta Advanced Education and Technology (ASRIP), Queen's University, University of Alberta, Carleton University, the Canada First Research Excellence Fund, the Arthur B. McDonald Canadian Astroparticle Physics Research Institute, DGAPA-UNAM (PAPIIT No. IA100118) and Consejo Nacional de Ciencia y Tecnología (CONACyT, Mexico, Grants No. 252167 and No. A1-S-8960), the European Research Council (ERC StG 279980), the UK Science & Technology Facilities Council (STFC) (ST/K002570/1 and ST/R002908/1), and the Leverhulme Trust (ECF-20130496). Support from the Rutherford Appleton Laboratory Particle Physics Division, STFC and SEPNet PhD is acknowledged. We thank SNOLAB and its staff for support through underground space, logistical and technical services. SNOLAB operations are supported by CFI and the Province of Ontario MRI, with underground access provided by Vale at the Creighton mine site. We thank Compute Canada, Calcul Québec, the Centre for Advanced Computing at Queen's University, and the Computational Centre for Particle and Astrophysics (C2PAP) at the Leibniz Supercomputer Centre (LRZ) for providing the computing resources required for this work.

[1] N. Aghanim *et al.* (Planck Collaboration), Planck 2018 results. VI. Cosmological parameters, arXiv:1807.06209.
[2] G. Bertone, D. Hooper, and J. Silk, Particle dark matter: evidence, candidates and constraints, Phys. Rep. **405**, 279 (2005).
[3] J. L. Feng, Dark matter candidates from particle physics and methods of detection, Annu. Rev, Astron. Astrophys. **48**, 495 (2010).
[4] M. W. Goodman and E. Witten, Detectability of certain dark-matter candidates, Phys. Rev. D **31**, 3059 (1985).
[5] E. Aprile *et al.* (XENON Collaboration), Dark Matter Search Results from a One Ton-Year Exposure of XENON1T, Phys. Rev. Lett. **121**, 111302 (2018).
[6] P.-A. Amaudruz *et al.* (DEAP-3600 Collaboration), First Results From The DEAP-3600 Dark Matter Search With Argon at SNOLAB, Phys. Rev. Lett. **121**, 071801 (2018).
[7] P. Agnes *et al.* (DarkSide Collaboration), DarkSide-50 532-day dark matter search with low-radioactivity argon, Phys. Rev. D **98**, 102006 (2018).
[8] M. G. Boulay and A. Hime, Technique for direct detection of weakly interacting massive particles using scintillation time discrimination in liquid argon, Astropart. Phys. **25**, 179 (2006).
[9] P.-A. Amaudruz *et al.*, Measurement of the scintillation time spectra and pulse-shape discrimination of low-energy β and nuclear recoils in liquid argon with DEAP-1, Astropart. Phys. **85**, 1 (2016).
[10] P.-A. Amaudruz *et al.* (DEAP-3600 Collaboration), Design and construction of the DEAP-3600 dark matter detector, Astropart. Phys. **108**, 1 (2019).
[11] P.-A. Amaudruz *et al.* (DEAP-3600 Collaboration), In-situ characterization of the Hamamatsu R5912-HQE photomultiplier tubes used in the DEAP-3600 experiment, Nucl. Instrum. Methods Phys. Res., Sect. A **922**, 373 (2019).
[12] R. Francini, J. E. Grindlay, B. Allen, J. Hong, S. Barthelmy, J. Braga, F. D'Amico, and R. E. Rothschild, Tetraphenyl-butadiene films: VUV-Vis optical characterization from room to liquid argon temperature, J. Instrum. **8**, C09010 (2013).
[13] B. Broerman *et al.*, Application of the TPB wavelength shifter to the DEAP-3600 spherical acrylic vessel inner surface, J. Instrum. **12**, P04017 (2017).
[14] P. Giampa, On the DEAP-3600 resurfacing, AIP Conf. Proc. **1921**, 070005 (2018).
[15] T. Lindner, DEAP-3600 data acquisition system, J. Phys. Conf. Ser. **664**, 082026 (2015).
[16] T. Bolton *et al.*, RAT (is an Analysis Tool) User's Guide, RAT (is an Analysis Tool) User's Guide (2018), https://rat.readthedocs.io.
[17] R. Brun and F. Rademakers, ROOT—An object oriented data analysis framework, Nucl. Instrum. Methods Phys. Res., Sect. A **389**, 81 (1997), New Computing Techniques in Physics Research V.
[18] S. Agostinelli *et al.*, Geant4—a simulation toolkit, Nucl. Instrum. Methods Phys. Res., Sect. A **506**, 250 (2003).
[19] M. Akashi-Ronquest *et al.*, Improving photoelectron counting and particle identification in scintillation detectors with Bayesian techniques, Astropart. Phys. **65**, 40 (2015).
[20] A. Butcher, L. Doria, J. Monroe, F. Retière, B. Smith, and J. Walding, A method for characterizing after-pulsing and dark noise of PMTs and SiPMs, Nucl. Instrum. Methods Phys. Res., Sect. A **875**, 87 (2017).
[21] M. Burghart, Background suppression through pulse shape analysis in the DEAP-3600 dark matter detector, Master's thesis, Technical University of Munich, 2018.
[22] A. Butcher, Searching for dark matter with DEAP-3600, Ph.D. thesis, Royal Holloway, University of London, 2015.
[23] T. Heindl, T. Dandl, M. Hofmann, R. Krücken, L. Oberauer, W. Potzel, J. Wieser, and A. Ulrich, The scintillation of liquid argon, Europhys. Lett. **91**, 62002 (2010).
[24] C. Stanford, S. Westerdale, J. Xu, and F. Calaprice, Surface background suppression in liquid argon dark matter detectors using a newly discovered time component of tetraphenyl-butadiene scintillation, Phys. Rev. D **98**, 062002 (2018).
[25] M. Wang, G. Audi, F. G. Kondev, W. J. Huang, S. Naimi, and X. Xu, The AME2016 atomic mass evaluation (II). Tables, graphs and references, Chin. Phys. C **41**, 030003 (2017).
[26] J. Calvo *et al.* (ArDM Collaboration), Backgrounds and pulse shape discrimination in the ArDM liquid argon TPC, J. Cosmol. Astropart. Phys. 12 (2018) 011.

[27] J. Kostensalo, J. Suhonen, and K. Zuber, Spectral shapes of forbidden argon β decays as background component for rare-event searches, J. Phys. G **45**, 025202 (2018).
[28] J. P. Davidson, The first forbidden shape factor and the $f_n t$ products for beta-decay, Phys. Rev. **82**, 48 (1951).
[29] M. Morita, Theory of beta decay, Progr. Theor. Exp. Phys. **26**, 1 (1963).
[30] L. Hayen, N. Severijns, K. Bodek, D. Rozpedzik, and X. Mougeot, High precision analytical description of the allowed β spectrum shape, Rev. Mod. Phys. **90**, 015008 (2018).
[31] H. Cao *et al.* (SCENE Collaboration), Measurement of scintillation and ionization yield and scintillation pulse shape from nuclear recoils in liquid argon, Phys. Rev. D **91**, 092007 (2015).
[32] T. R. Pollmann, Estimating the efficiency turn-on curve for a constant-threshold trigger without a calibration dataset, Eur. Phys. J. C **79**, 322 (2019).
[33] J. McLaughlin, Corrections to signal saturation on the DEAP-3600 dark matter search, Master's thesis, Queen's University, 2018.
[34] A. C. Sinnock and B. L. Smith, Refractive indices of the condensed inert gases, Phys. Rev. **181**, 1297 (1969).
[35] E. Grace, A. Butcher, J. Monroe, and J. A. Nikkel, Index of refraction, Rayleigh scattering length, and Sellmeier coefficients in solid and liquid argon and xenon, Nucl. Instrum. Methods Phys. Res., Sect. A **867**, 204 (2017).
[36] B. J. P. Jones, C. S. Chiu, J. M. Conrad, C. M. Ignarra, T. Katori, and M. Toups, A measurement of the absorption of liquid argon scintillation light by dissolved nitrogen at the part-per-million level, J. Instrum. **8**, P07011 (2013).
[37] Q. Chen J. Cheng, Q. Yue, Y. Du, and W. Liu, Scintillation yield and scintillation time dependence in gaseous Argon with different purities, in *2013 IEEE Nuclear Science Symposium and Medical Imaging Conference (2013 NSS/MIC)* (IEEE, New York, 2013), https://dx.doi.org/10.1109/NSSMIC.2013.6829471.
[38] R. Acciarri *et al.*, Effects of Nitrogen and Oxygen contamination in liquid Argon, Nucl. Phys. B, Proc. Suppl. **197**, 70 (2009).
[39] C. Amsler, V. Boccone, A. Büchler, R. Chandrasekharan, C. Regenfus, and J. Rochet, Luminescence quenching of the triplet excimer state by air traces in gaseous argon, J. Instrum. **3**, P02001 (2008).
[40] J. Calvo *et al.* (ArDM Collaboration), Measurement of the attenuation length of argon scintillation light in the ArDM LAr TPC, Astropart. Phys. **97**, 186 (2018).
[41] W. B. Wilson, R. T. Perry, W. S. Charlton, T. A. Parish, and E. F. Shores, SOURCES: a code for calculating (α, n), spontaneous fission, and delayed neutron sources and spectra, Radiation Protection Dosimetry **115**, 117 (2005).
[42] S. Westerdale and P. D. Meyers, Radiogenic neutron yield calculations for low-background experiments, Nucl. Instrum. Methods Phys. Res., Sect. A **875**, 57 (2017).
[43] B. Aharmim *et al.* (SNO Collaboration), Measurement of the cosmic ray and neutrino-induced muon flux at the Sudbury neutrino observatory, Phys. Rev. D **80**, 012001 (2009).
[44] D.-M. Mei and A. Hime, Muon-induced background study for underground laboratories, Phys. Rev. D **73**, 053004 (2006).
[45] R. D. Cousins and V. L. Highland, Incorporating systematic uncertainties into an upper limit, Nucl. Instrum. Methods Phys. Res., Sect. A **320**, 331 (1992).
[46] R. Agnese *et al.* (SuperCDMS Collaboration), Results From The Super Cryogenic Dark Matter Search Experiment At Soudan, Phys. Rev. Lett. **120**, 061802 (2018).
[47] D. S. Akerib *et al.* (LUX Collaboration), Results From A Search For Dark Matter In The Complete LUX Exposure, Phys. Rev. Lett. **118**, 021303 (2017).
[48] X. Cui *et al.* (PandaX-II Collaboration), Dark Matter Results From 54-Ton-Day Exposure Of PandaX-II Experiment, Phys. Rev. Lett. **119**, 181302 (2017).
[49] C. McCabe, Astrophysical uncertainties of dark matter direct detection experiments, Phys. Rev. D **82**, 023530 (2010).
[50] M. Hoferichter, P. Klos, J. Menéndez, and A. Schwenk, Analysis strategies for general spin-independent WIMP-nucleus scattering, Phys. Rev. D **94**, 063505 (2016).
[51] A. L. Fitzpatrick, W. Haxton, E. Katz, N. Lubbers, and Y. Xu, The effective field theory of dark matter direct detection, J. Cosmol. Astropart. Phys. 02 (2013) 004.